

Probing the coverage of nanoparticles by biomimetic membranes through nanoplasmonics

Jacopo Cardellini^{1,2}, Andrea Ridolfi^{1,2,3,4}, Melissa Donati¹, Valentina Giampietro¹, Mirko Severi¹, Marco Brucale^{2,3}, Francesco Valle^{2,3}, Paolo Bergese^{2,5,6}, Costanza Montis^{1,2}, Lucrezia Caselli^{1,2,7}, and Debora Berti^{1,2*}*

1 Department of Chemistry “Ugo Schiff”, University of Florence, Florence, Italy

2 CSGI, Consorzio Sistemi a Grande Interfase, University of Florence, Sesto Fiorentino, Italy

3 Istituto per lo Studio dei Materiali Nanostrutturati, Consiglio Nazionale delle Ricerche, 40129 Bologna, Italy

4 Department of Physics and Astronomy and LaserLaB Amsterdam, Vrije Universiteit Amsterdam, Amsterdam, The Netherlands (current affiliation)

5 Department of Molecular and Translational Medicine, University of Brescia, Brescia, Italy

6 Consorzio Interuniversitario Nazionale per la Scienza e la Tecnologia dei Materiali, Florence, Italy

7 Department of Physical Chemistry 1, University of Lund, SE-22100 Lund, Sweden (current affiliation)

*E-mails: debora.berti@unifi.it, lucrezia.caselli@fkem1.lu.se (corresponding authors)

Keywords

membrane-coated nanoparticles, gold nanoparticles, nanoplasmonics, biomimetic nanoparticles, silica nanoparticles, nano-bio interface, Extracellular Vesicles, Nanomedicine

Abstract

Although promising for biomedicine, the clinical translation of inorganic nanoparticles (NPs) is limited by low biocompatibility and stability in biological fluids. A common strategy to circumvent this drawback consists in disguising the active inorganic core with a lipid bilayer coating, reminiscent of the structure of the cell membrane to redefine the chemical and biological identity of NPs. While recent reports introduced membrane-coating procedures for NPs, a robust and accessible method to quantify the integrity of the bilayer coverage is not yet available. To fill this gap, we prepared SiO₂ nanoparticles (SiO₂NPs) with different membrane coverage degrees and monitored their interaction with AuNPs by combining microscopic, scattering, and optical techniques. The membrane-coating on SiO₂NPs induces spontaneous clustering of AuNPs, whose extent depends on the coating integrity. Remarkably, we discovered a linear correlation between the membrane coverage and a spectral descriptor for the AuNPs' plasmonic resonance, spanning a wide range of coating yields. These results provide a fast and cost-effective assay to monitor the compatibilization of NPs with biological environments, essential for bench tests and scale-up. In addition, we introduce a robust and scalable method to prepare SiO₂NPs/AuNPs hybrids through spontaneous self-assembly, with a high-fidelity structural control mediated by a lipid bilayer.

1. Introduction

Over the last decades, numerous efforts have been devoted to the exploitation of the unique properties of inorganic nanoparticles (NPs) for biomedical applications. Despite a large number of NPs developed for biomedical purposes and reports illustrating their in-vitro potential, the route for effective clinical translation is still minimal due to multiple issues¹⁻⁵, including poor colloidal stability and limited circulation time in biological fluids, cytotoxic effects, poor targeting ability and uncontrolled accumulation in specific tissues, which eventually leads to low efficacy and unwanted side effects.⁶ In a simplistic view, these drawbacks could be considered to be related to a general issue, i.e. the inherent exogenous, synthetic nature of inorganic NPs, and their size, which – being close to that of biomolecules and biological assemblies – can lead to unpredictable behavior when inserted into a biological environment. Coating NPs with a lipid membrane of either synthetic or natural origin is one of the most promising strategies to circumvent this issue, which led to a new class of nanomaterials, i.e., membrane-camouflaged biomimetic NPs. While retaining the physicochemical properties of the core (inorganic) material, the lipid shell of these systems provides biomimetic surface functions, such as immune escape ability and modulation, specific molecular recognition and targeting, enhanced cell adhesion, reduced toxicity, and long circulation time.⁷⁻¹² Among the possible sources for membrane camouflaging, synthetic lipid bilayers, whose composition can be conveniently tailored to resemble that of biological membranes, are commonly employed as bioinspired coatings to improve the biocompatibility and pharmacokinetics of NPs,^{13,14} as well as to enhance their colloidal stability¹⁵. Lipid bilayers can be easily functionalized to introduce targeting properties^{16,17}, steering the carriers towards specific sites, protecting them from the biological environment, and preventing the uncontrolled leakage of drugs.¹⁴ More sophisticated coatings^{18,19}, employing natural cell membranes (e.g., of red²⁰⁻²⁴ and white²⁵⁻²⁷ blood

cells, cancer cells^{28–30}, stem cells³¹, platelets^{32,33}, and bacterial walls^{34–36}), are currently the focus of intensive research, which has already led to the development of hybrid NPs with superior properties for drug delivery^{37–39}, in vitro imaging^{20,40,41}, diagnosis and treatment of cancer^{42–44}, bacterial infections^{45,46} and other diseases⁴⁷, anticancer vaccination⁴⁸ and detection of viral pathogens⁴⁹. In the palette of natural camouflages, the biomembrane of Extracellular Vesicles' (EVs') represents one of the latest -and more promising- frontiers.⁵⁰ EVs are biogenic vesicles naturally secreted by cells, containing lipids, proteins, nucleotides, and metabolites in the inner pool.⁵¹ As compared to other natural membrane coatings, EVs provide unmet targeting abilities, which are connected to their role in cell-cell chemical communication as nano-shuttles for proteins, lipids, and RNA^{52,53,54}. Provided by its endogenous origin, the EV membrane also offers near non-immunogenicity, resistance to macrophage uptake^{55,53}, and the ability to cross the blood-brain barrier^{57,58}, as well as enhanced endocytosis efficiency.⁵⁹ Coating NPs with the EVs membrane has recently proved as a powerful tool to achieve immune evasion-mediated targeting⁶⁰ and selective accumulation at the tumor site^{60,61}, e.g., through receptor-mediated endocytosis.⁶²

Despite the consistent growth of the library of available membrane-coated NPs, achieving complete membrane coverage and developing efficient and reliable methods to quantify its integrity remain significant hurdles. An incomplete membrane coating drastically decreases the colloidal stability of NPs^{63–65}, and may promote cargo leakage in drug-delivery systems⁶⁶. Moreover, the integrity of the membrane coating modulates the efficiency of macrophage clearance⁶⁷ and affects the internalization mechanism of biomimetic NPs⁶⁸, as well as their biomedical functions^{69–71}.

So far, the characterization of the coating integrity has primarily relied on microscopy techniques (e.g., Electron, Confocal Laser Scanning, and Atomic Force microscopies)^{72–74}, Dynamic Light Scattering (DLS)⁷², and Zeta Potential measurements^{75–77}. However, microscopy techniques do not provide ensemble-averaged characterization and generally require specialized equipment and ad-hoc sample preparation. On the other side, scattering-based methods and other traditional approaches (e.g., colloidal stability test in phosphate-buffered saline or fetal bovine serum⁶⁸, and sodium dodecyl sulfate-polyacrylamide gel electrophoresis^{75,78}) fail in providing a quantitative estimate of the coating extent. More sophisticated techniques, such as mass spectrometry (MS) or liquid chromatography-tandem MS^{79–81}, only give a rough estimation of the coating degree, i.e., heavily affected by strong assumptions on the morphology and structure of the coating itself.

Here, we report a new colorimetric and spectrophotometric method for quantitatively assessing the membrane coating extent based on the plasmonic properties of citrate-coated gold nanoparticles (AuNPs). AuNPs spontaneously interact with free-standing lipid bilayers, leading to membrane adhesion⁸² and AuNPs clustering^{83–89}. Recently, we have shown how the spontaneous clustering of AuNPs on synthetic and natural lipid vesicles (such as EVs) can be exploited to gain information on the characteristics of the vesicles themselves, such as their concentration⁹⁰, stiffness^{91,92}, and the presence of protein contaminants⁹³. Overall, AuNPs plasmonic properties are emerging as convenient, highly sensitive, and robust probes for lipid interfaces. Given these unique properties, we here test the ability of AuNPs to probe and possibly quantify the membrane coating degree on the surface of inorganic NPs. To this purpose, we prepare biomimetic NPs with an inorganic silica core and a synthetic membrane shell, whose composition mimics the typical one of EVs. Through a combination of structural and spectrophotometric techniques, we investigate the interaction of

such membrane-coated SiO₂NPs (M-SiO₂NPs) with AuNPs, as a function of the membrane coating integrity. Finally, we leverage these findings to estimate the extent of the lipid coverage of M-SiO₂NPs, through a simple and fast colorimetric assay.

2. Materials and Methods

2.1 Materials

Tetrachloroauric (III) acid ($\geq 99.9\%$) was provided by Sigma-Aldrich (St. Louis, MO). 1,2-Dioleoyl-sn-glycero-3-phosphocholine (DOPC) ($\geq 99.0\%$), N-palmitoyl-D-erythro-sphingosylphosphorylcholine (sphingomyelin) ($\geq 98.0\%$), and cholesterol ($\geq 99.0\%$) were provided by Avanti Polar Lipids. Sucrose, sodium chloride (NaCl) ($\geq 99.5\%$), sodium citrate (Na₃C₆H₅O₇) ($\geq 99.9\%$), and calcium chloride (CaCl₂) ($\geq 99.999\%$) were provided by Sigma Aldrich. All chemicals were used as received. Milli-Q-grade water was used in all preparations. Silica Nanoparticles were provided by HiQ-Nano (Arnesano, Lecce, Italy) and are stable in an aqueous buffer and are characterized by a hydrophilic surface with terminal Si-OH functional groups.

2.2 Preparation of SiO₂NPs

The commercial batch was thoroughly homogenized by vortexing, followed by 30 min bath sonication before use. Subsequently, it was diluted in milliQ water to obtain a final SiO₂ concentration of 1.6 mg/mL right before mixing with liposomes.

2.3 Preparation of liposomes

To prepare the EVs-mimicking liposomes, the proper amount of DOPC, Sphingomyelin, and cholesterol was dissolved in chloroform (0.87/0.37/1 mol%/mol%), and a lipid film was obtained by evaporating the solvent under a stream of nitrogen and overnight vacuum drying. The film was then swollen and suspended in a warm (40 °C) water solution of sucrose (650 mM), sodium chloride (150 mM), and sodium citrate (10 mM) by vigorous vortex mixing to obtain a final lipid concentration of 7 mg/ml. The resultant multilamellar vesicles (MVL) in water were subjected to 10 freeze–thaw cycles and extruded 10 times through two stacked polycarbonate membranes with a 100 nm pore size at room temperature to obtain unilamellar vesicles (ULV) with a narrow and reproducible size distribution. The filtration was performed with the Extruder (Lipex Biomembranes, Vancouver, Canada) through Nucleopore membranes.

2.4 Preparation of membrane-coated Silica Nanoparticles (M-SiO₂NPs)

To prepare fully coated SiO₂-NPs, 1 mL of a dispersion of uncoated SiO₂-NPs in ultrapure water (1.6 mg/mL) was mixed with 1 mL of liposomes dispersion (7 mg/mL) at high stoichiometric excess of liposomes (approximately 1/50 SiO₂-NPs/liposomes number ratio), formed in an aqueous environment with high osmolality (650 mM sucrose, 10 mM Sodium Citrate, 150 mM NaCl, 10 mM CaCl₂). The formation of the lipid coating on SiO₂NPs starts with the adhesion of the vesicles on the SiO₂NPs surface due to Van der Waals interactions; this is followed by membrane rupture driven by the transmembrane gradient of osmotic pressure between the inner aqueous pool and the dispersing medium (SiO₂NPs were initially dispersed in ultrapure water).

The excess of intact liposomes was then removed through centrifugation (6000 rpm x 30 min each), after which the supernatant was discarded, and the precipitate (containing M-SiO₂NPs) collected and redispersed in ultrapure water. This last step was repeated 6 times to fully remove the excess of intact vesicles. To account for possible material loss during the centrifugation cycles, the final concentration of M-SiO₂NPs was quantified by ICP-AES (see section S2.3).

To prepare M-SiO₂-NPs with different degrees of coverage we employed the same protocol varying the initial SiO₂NPs/vesicle ratio. Specifically, 1 mL SiO₂-NPs in ultrapure water (1.6 mg/mL) was mixed with 1 mL of liposomes properly diluted to obtain SiO₂NPs/vesicle ratios of approximately 1/15, 1/10, 1/5, 1/3, and 1/1. The intact liposomes were removed through centrifugation (6000 rpm x 30 min each), and the precipitate was collected and redispersed in 1 mL of ultrapure water.

2.5 Synthesis of AuNPs

Anionic gold nanospheres (AuNPs) of 12 nm in size were synthesized according to the Turkevich–Frens method.^{94,95} Briefly, 20 mL of a 1 mM HAuCl₄ aqueous solution was brought to the boiling temperature under constant and vigorous magnetic stirring. 2 mL of a 1% citric acid solution were then added to the mixture. The solution was further boiled for 10 min until it acquired a deep red color. The nanoparticle solution was then slowly cooled to room temperature.

2.6 Cryo-EM

3 μL of each sample at a SiO_2NPs concentration of 1.15 nM were applied on glow-discharged Quantifoil Cu 300 R2/2 grids. The samples were plunge-frozen in liquid ethane using an FEI Vitrobot Mark IV (Thermo Fisher Scientific) instrument. The excess liquid was removed by blotting for 1 s (blot force of 1) using filter papers under 100% humidity and at 10 °C. Cryo-EM data were collected at the Florence Center for Electron Nanoscopy (FloCEN), University of Florence (Italy), on a Glacios (Thermo Fisher Scientific) instrument at 200 kV equipped with a Falcon III detector operated in the counting mode. Images were acquired using EPU software with a physical pixel size of 2.5 Å and a total electron dose of $\sim 50 \text{ e}^-/\text{Å}^2$ per micrograph.

2.7 Atomic Force Microscopy (AFM)

NPs were deposited on top of poly-L-lysine (PLL) coated glass coverslips. All reagents were purchased from Sigma-Aldrich Inc (www.sigmaaldrich.com) unless otherwise stated. Menzel Gläser coverslips were cleaned in Piranha solution for 2h and washed in a sonicator bath (Elmasonic Elma S30H) for 30' in acetone, followed by 30' in isopropanol and 30' in ultrapure water (Millipore Simplicity UV). Before each experiment, glass coverslips were treated with air plasma (Pelco Easiglow) and immersed into a 0.01 mg/mL PLL solution in Borate buffer (pH 8.33) at room temperature for 30 minutes. After being thoroughly rinsed with ultrapure water and dried with nitrogen, the coverslips were ready to be used for the AFM experiments. A 10 μl droplet of the SiO_2NPs dispersion was deposited on top of the coverslips and left equilibrating for 15 minutes before being inserted into the AFM fluid cell. The concentrations of SiO_2NP dispersions were

adjusted via trial and error to avoid the formation of NP-clusters, which would ultimately prevent the quantitative determination of their morphology. AFM experiments were performed in PeakForce mode at room temperature on a Bruker Multimode 8 equipped with Nanoscope V electronics, a sealed fluid cell, a type JV piezoelectric scanner, and Bruker SNL10-A probes (with nominal tip radius 2-12 nm and spring constant 0.35 N/m), calibrated according to the thermal noise method⁹⁶. A 50 mM MgCl₂, 100 mM KCl solution was used as imaging buffer in order to reduce the electrical double layer (EDL) interaction region between the AFM tip and the NPs⁹⁷. NP height was used to obtain the respective size distributions; given that NPs are spherical rigid objects, their height coincides with the NP diameter and, being unaffected by tip convolution effects, represents a reliable parameter for size estimation.

2.8 Dynamic Light Scattering (DLS) and ζ -Potential

DLS measurements at $\theta = 90^\circ$ and the ζ -potential determination were performed using a Brookhaven Instrument 90 Plus (Brookhaven, Holtsville, NY). Each measurement was an average of 10 repetitions of 1 min each, and measurements were repeated 10 times. The autocorrelation functions (ACFs) were analyzed through cumulant fitting stopped at the second order for samples characterized by a single monodisperse population, allowing an estimate of the hydrodynamic diameter of particles and the polydispersity index. ζ -potentials were obtained from the electrophoretic mobility u according to the Helmholtz–Smoluchowski equation $\zeta = \left(\frac{\eta}{\epsilon}\right) \times \mu$ (1), where η is the viscosity of the medium and ϵ is the dielectric permittivity of the dispersing medium. The ζ -potential values are reported as averages from 10 measurements.

2.9 Inductively Coupled Plasma - Atomic Emission Spectrometry (ICP-AES)

The determination of Si and P content in the samples was performed in triplicate by using a Varian 720-ES Inductively Coupled Plasma Atomic Emission Spectrometer (ICP-AES). An accurately measured amount of each sample was diluted to a final volume of 5 mL with 1% suprapure HNO₃ obtained by sub-boiling distillation. Each sample was thus spiked with 100 μL of Ge 50 mg/L standard solution used as the internal standard. Calibration standards were prepared by gravimetric serial dilution from a commercial stock standard solution of Si and P at 1000 mg L⁻¹. The analytic wavelengths used for Si and P determination were 251.611 and 213.618 nm, respectively, whereas for Ge we used the line at 209.426 nm. The operating conditions were optimized to obtain the maximum signal intensity, and between each sample, a rinse solution constituted of 2% v/v HNO₃ was used to avoid memory effects.

2.10 UV-vis spectroscopy

UV-vis spectra were recorded with a Cary 3500 UV-vis spectrophotometer. 50 μL of either naked SiO₂NPs or M-SiO₂NPs (at a SiO₂ concentration of 1.15 nM with different degrees of coverage) were mixed with 300 μL of 6.13 nM AuNPs and incubated for 10 minutes at room temperature in PMMA UV-vis micro cuvettes (maximum volume 1.5 mL). Then, 700 μL of MilliQ water were added to the samples, and after 10 minutes, the spectra were simultaneously recorded with a multiple sample holder in the spectral range 350-800 nm.

2.11 Small Angle X-ray Scattering

M-SiO₂NPs/AuNPs hybrids were characterized at the SAXS beamline of the synchrotron radiation source Elettra (Trieste, Italy), which was operated at 2 GeV and a 300mA ring current. The experiments were carried out with $\lambda = 1.5 \text{ \AA}$, and the SAXS signal was detected with a Pilatus 3 1M detector in the q -range from 0.009 to 0.7 \AA^{-1} . The SAXS curves were recorded in a glass capillary.

3. Results and Discussion

3.1. Formation of biomimetic membrane-coated SiO₂NPs (M-SiO₂NPs)

As model inorganic particles, we selected commercial anionic SiO₂NPs, given their well-known surface chemistry and the wide range of applications in biomedical research^{98,99}. To form the lipid coating, we used DOPC (1,2-dioleoyl-sn-glycero-3-phosphocholine)/Sphingomyelin/Cholesterol (0.87/0.38/1.00 mol%) vesicles, characterized by an average hydrodynamic diameter of 110 nm (PDI 0.150) and a ζ -potential of $-15.2 \pm 1.3 \text{ mV}$ (see section S2 of SI). Composition-wise, these synthetic membranes do not account for the complexity observed in biomembranes, which typically feature an impressive number of different proteins, lipids and (in the case of EVs) nucleic acids. Nevertheless, the above lipid composition has been specifically selected to retain the hallmark feature of EVs membranes, shared among EVs of different sources and biological

functions, i.e., the typical enrichment in sphingomyelin and cholesterol, as compared to parental cells.¹⁰⁰ Thus, in spite being highly simplified, these synthetic systems can still represent effective models for the prototypical features of the lipid membrane of EVs. The lipid coating of SiO₂NPs was obtained through a slight modification of a well-established protocol¹⁰¹ (described in the Materials and Methods section). Briefly, this method relies upon mixing SiO₂NPs in ultrapure water with a high stoichiometric excess of liposomes ($\geq 1/50$ SiO₂NPs/liposomes number ratio), formed in an aqueous medium with high osmolality. The adhesion of vesicles on the SiO₂NPs surface, driven by Van der Waals attractive forces, is quickly followed by membrane rupture, triggered by the transmembrane gradient of osmotic pressure between the inner aqueous pool of vesicles and the dispersing medium. M-SiO₂NPs were imaged through Cryogenic electron microscopy (Cryo-EM), with Figures 1a and 1b displaying representative Cryo-EM images at different magnifications. While only very few intact vesicles appear to sit onto the SiO₂ surface (see Figure 1a, top part, and section S2.1 for additional images), most of SiO₂NPs are either totally or partially (Fig. 1b red arrows) surrounded by a nanometric layer, closely following the particle morphology, with an electron density that is intermediate between the ones of SiO₂ and the surrounding medium. This layer can be reasonably identified as the bilayer, originally constituting the lipid membrane of vesicles. To gain additional information on the thickness of the surrounding layer, the samples were also imaged by liquid-Atomic Force Microscopy (AFM). Representative AFM images of SiO₂NPs and M-SiO₂NPs are displayed in Figure S2.2, while Figure 1c reports the size distributions obtained for the two samples; the average diameter for the SiO₂NPs is 125 ± 10 nm, while the one of M-SiO₂NPs is 140 ± 15 nm. The 15 nm difference between the two average diameters is compatible with the presence of a lipid bilayer entirely covering most of the particles of the M-SiO₂NP sample. In addition, we characterized the lipid coating at an ensemble-averaged

level, performing DLS and ζ -Potential measurements (Figure 1d). The DLS autocorrelation functions for bare and M-SiO₂NPs (Figure 1d) were analyzed through a cumulant fitting stopped at the second order¹⁰². The inset in Figure 1d summarizes the main results. The hydrodynamic diameter of uncoated SiO₂NPs, inferred from the corresponding autocorrelation function, is 165 nm (PDI 0.067). It is worth highlighting that the hydrodynamic size of SiO₂NPs is remarkably larger (~40 nm) than the primary particle diameter determined by AFM, which is in line with previous reports¹⁰³. In contrast, the autocorrelation function of M-SiO₂NPs decays at longer times, consistent with an increase of hydrodynamic diameter up to 210 nm (PDI 0.1), which is compatible with an extensive formation of a lipid bilayer on the SiO₂NPs. Moreover, the characteristic ζ -Potential increases from -40 ± 1 mV (for SiO₂NPs) to -22 ± 1 mV (for M-SiO₂NPs), which is very close to the one of liposomes (-15 ± 1 mV), further confirmation of the effective lipid coverage of the SiO₂NPs' surface. Lastly, we quantified the extent of the SiO₂ surface covered by the lipid bilayer employing Inductively Coupled Plasma-Atomic Emission Spectrometry (ICP-AES). This technique allows for exact quantification of the Si and P atoms in the final M-SiO₂NPs samples, from which the ratio between the covered and bare SiO₂ surfaces can be inferred through simple geometrical models (see section S5.1 in SI). It is worth stressing that these models heavily rely on specific assumptions about the packing of lipid molecules within the membrane formed on SiO₂ (see section 2.3 of SI); consequently, the technique can only provide a rough estimation of the degree of coverage of the SiO₂NPs surface. Through this approach, a coverage % of 88 ± 8 was estimated for the sample reported in Fig 1.

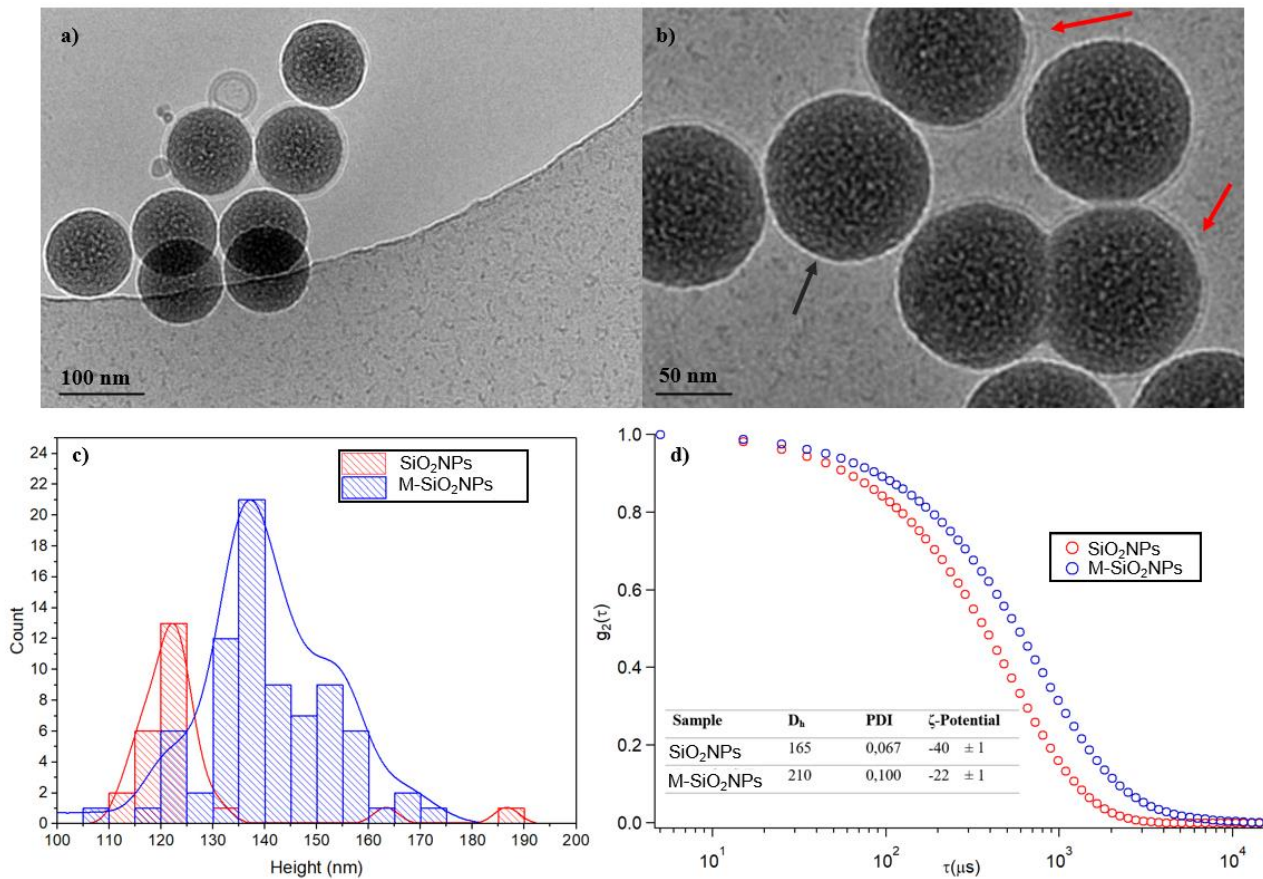


Figure 1. a) and b) Cryo-EM images of M-SiO₂NPs at different magnifications (red and black arrows identify coated and uncoated areas of M-SiO₂NPs, respectively); c) Size distribution of SiO₂NPs (red) and M-SiO₂NPs (blue) obtained by liquid-AFM imaging; d) Autocorrelation functions of 0.08 mg/mL water dispersion of SiO₂NPs (red) and M-SiO₂NPs (blue). The inset shows the hydrodynamic diameter (extrapolated by a cumulant fitting) and the ζ -potential values of each sample.

3.2. The interaction of M-SiO₂NPs with citrate-coated gold nanoparticles

Once the formation of M-SiO₂NPs was demonstrated via different complementary techniques, as discussed in the previous paragraph, we tested the possibility of probing the lipid layer covering

the NPs utilizing the plasmonic properties of AuNPs. To this purpose, 1.15 nM bare SiO₂NPs (control sample) were first challenged by 6.13 nM Turkevich-Frens AuNPs with an average diameter of 12 nm (PDI 0.095) and -35 ± 3 mV ζ -Potential (see section S3 of SI for AuNPs characterization), for a final SiO₂NPs/AuNPs number ratio of $\sim 1/30$. The sample was imaged via Cryo-EM (Figure 2a), showing that AuNPs do not interact with bare SiO₂NPs, which is expected for the electrostatic repulsion between the two inorganic surfaces, both having a highly negative ζ -Potential. Conversely, when AuNPs are incubated with M-SiO₂NPs under the same conditions, a completely different effect is visible: as shown in Figure 2b (see also section S4.1 for additional images), AuNPs spontaneously cluster on M-SiO₂NPs, forming AuNPs-decorated M-SiO₂NPs composites. This phenomenon, which did not occur with the bare SiO₂NPs, is clearly induced by the presence of a lipid bilayer on the SiO₂ surface, which mediates the adhesion and clustering of AuNPs on M-SiO₂NPs. Cryo-TEM results were complemented by an ensemble-averaged characterization performed through DLS (see section S4.2 of SI), which provided the mean size and polydispersity of SiO₂NPs/AuNPs and M-SiO₂NPs/AuNPs mixed samples. This characterization showed no interaction between AuNPs and bare SiO₂NPs, testified by the presence of two distinct populations within the SiO₂NPs/AuNPs sample, whose sizes perfectly match the ones of free AuNPs (~ 20 nm) and free SiO₂NPs (~ 170 nm). In contrast, a single population of bigger size (~ 230 nm) was detected for the M-SiO₂NPs/AuNPs sample, consistent with the formation of composites in which M-SiO₂NPs are decorated by a layer of AuNPs. Remarkably, the clustering of AuNPs on M-SiO₂NPs led to an evident color change of the AuNPs dispersion from red to purple/blue (see insets of Figures 2c and 2d) within 10 minutes of incubation, which can be noticed by the naked eye and is connected to a variation of AuNPs' plasmonic properties. Conversely, bare SiO₂NPs do not induce significant color variations in the

AuNPs' dispersion. The corresponding spectral variations were quantified by means of UV-Vis spectroscopy (results displayed in Figures 2c and 2d). In line with visual observation, the interaction of AuNPs with bare SiO₂NPs does not significantly alter the plasmonic features of AuNPs, consisting of the characteristic plasmonic primary peak located at 520 nm (red trace). On the contrary, the interaction with M-SiO₂NPs causes a red-shift of the plasmon resonance peak of AuNPs and the occurrence of an additional red-shifted shoulder, a well-established signature of plasmon coupling^{91,92}, consistent with AuNPs aggregation. As already anticipated, a similar coupling of the plasmons of AuNPs has been observed for AuNPs interacting with natural or synthetic vesicles and has been found to be triggered by AuNPs adhesion to the lipid membrane^{82,90}, driven by Van der Waals interactions, and promoted by the bending ability of the membrane⁹⁰⁻⁹². Such phenomenon has been also conveniently used for determining the concentration, purity, and rigidity of such synthetic or natural vesicles^{54,104}. Here for the first time, we show that this phenomenon can also be activated on rigid nanoparticles (such as inorganic SiO₂NPs), thanks to the mediating action of a lipid bilayer covering their surface. The clustering of AuNPs on free-standing bilayers was previously found to be promoted by the bending ability of the lipid membrane^{88,90-92}; on the contrary, it was expected to be strongly suppressed (or fully prevented) for lipid interfaces formed on rigid supports (e.g., the inorganic core of NPs), where membrane bending ability is strongly reduced. To shed light on this aspect, we directly compared the UV-Vis spectra of AuNPs incubated with M-SiO₂NPs with the ones of AuNPs interacting with liposomes presenting the same membrane composition (see section S4.3 of SI); the results showed that the rigid core of SiO₂ strongly decreases the aggregation of AuNPs on the lipid membrane (likely due to the increment in the overall stiffness of M-SiO₂NPs composites with respect to pristine vesicles), without, however, completely preventing it. In fact, the clustering extent of

AuNPs on M-SiO₂NPs is sufficient to detect an apparent color change in AuNPs dispersion and, accordingly, a variation in the corresponding UV-Vis absorbance spectra.

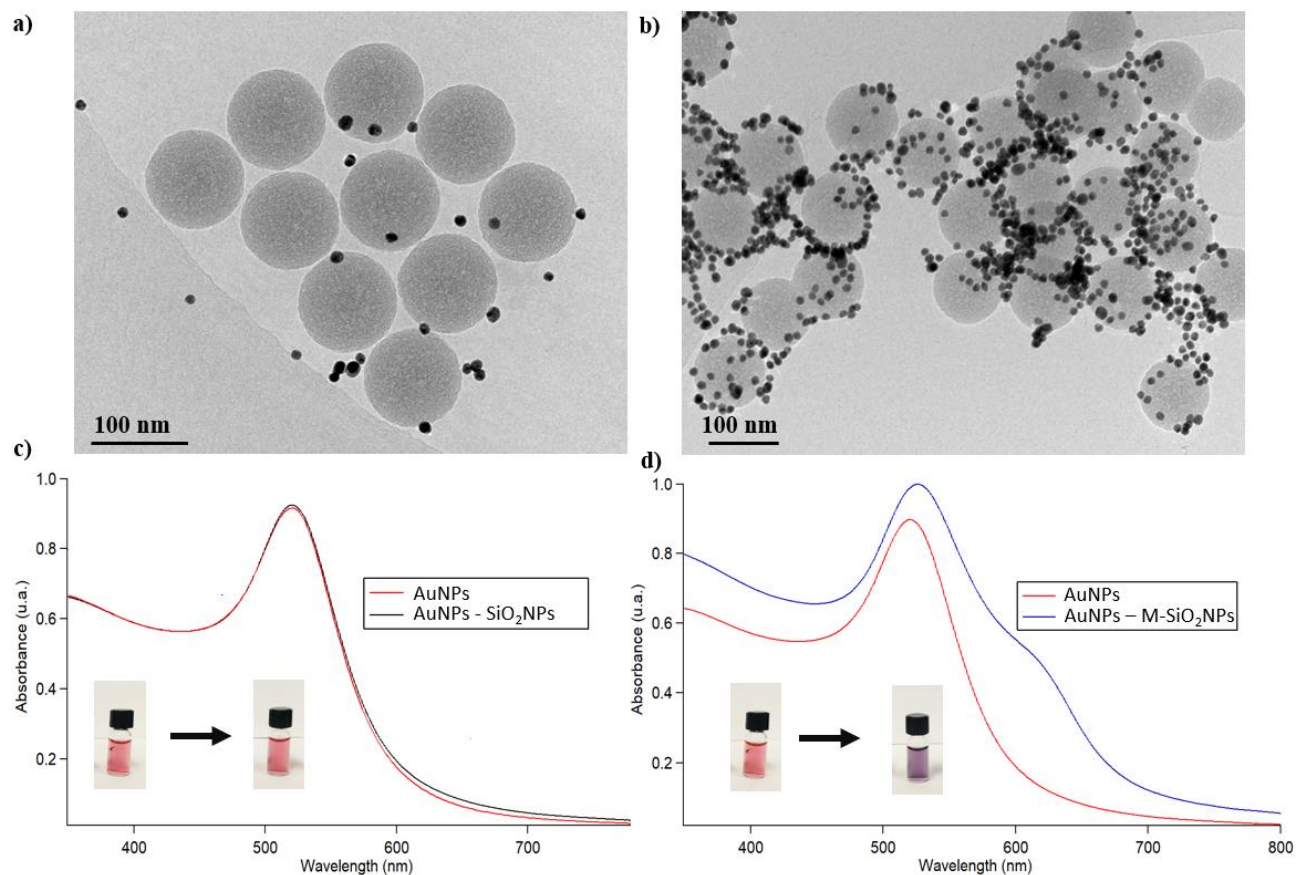


Figure 2. Cryo-EM images of (a) SiO₂NPs/AuNPs, (b) M-SiO₂NPs/AuNPs composites, and UV-visible spectra of AuNPs incubated with (c) SiO₂NPs and (d) M-SiO₂NPs. The UV-Vis spectrum of bare AuNPs (red curve) is also reported as a control sample. The visual appearance of AuNPs before and after the incubation with SiO₂NPs and M-SiO₂NPs is reported in the insets of the graphs. See also Figure S11 of SI for UV-Vis control spectra of SiO₂NPs and M-SiO₂NPs in the absence of AuNPs.

3.3 A nanoplasmonic assay to quantify lipid coverage in M-SiO₂NPs

Having demonstrated that the self-assembly of citrate-coated AuNPs occurs on lipid-coated SiO₂NPs and not on bare ones, we explored how the plasmonic variations of AuNPs are affected by the extent of lipid coverage of the SiO₂NPs. To this aim, we applied the same transmembrane osmotic shock-based protocol for synthesizing several SiO₂NPs samples with different degrees of coating (see Materials and Methods section). While a NP/vesicle ratio $\geq 1/50$ is required to obtain almost full coverage of the silica surface (i.e., $\sim 88\%$, see previous paragraphs), the coverage extent can be tuned by varying the SiO₂NP/vesicle ratio during incubation. Employing SiO₂NPs/vesicles ratios of 1/50, 1/15, 1/10, 1/5, 1/3, and 1/1, we realized different hybrids and characterized them through ICP-AES, DLS, and ζ -potential (see section 2.4). Table 1 provides a full overview of such characterization.

Sample	D _h (nm)	PDI	ζ -Potential (mV)	SiO ₂ NPs coverage
Vesicles	115	0.115	-11.2 \pm 1.1	/
SiO ₂ NPs	165	0.067	-40.2 \pm 0.9	0%
1/50	210	0.100	-22.7 \pm 1.3	88 \pm 8%
1/15	193	0.122	-26.2 \pm 1.2	68 \pm 7%
1/10	189	0.164	-28.6 \pm 0.7	60 \pm 6%
1/5	193	0.152	-30.3 \pm 1.4	53 \pm 5%
1/3	414	0.363	-37.1 \pm 3.2	33 \pm 3%
1/1	621	0.335	-36.5 \pm 3.5	13 \pm 1%

Increasing coverage

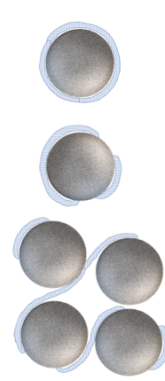


Table 1. Hydrodynamic diameter, PDI and ζ -potential values of SiO₂NPs, bare vesicles, and M-SiO₂NPs obtained using different SiO₂NPs-vesicles ratios. The last column reports the SiO₂NPs coverage percentage, calculated from the concentration of P and Si measured by ICP-AES for each composition (see SI section S2.3). The inset displays a schematic representation of how the coverage affects the size and stability of the hybrids.

The results obtained from ICP-AES measurements were used for a rough estimation of the coating degrees of SiO₂NPs (see SI section S2.3). The coating fraction ranged from 13% to 88% by increasing the number of vesicles employed in the incubation step. The size, colloidal stability, and surface charge of the M-SiO₂NPs with different coating degrees were assessed by DLS and ζ -Potential. The ζ -Potential of the M-SiO₂NPs decreases in a monotonous trend, passing from -23 ± 1 mV for the 1/50 SiO₂NPs/vesicle ratio to -37 ± 4 mV for the 1/1 one, which is very close to the value obtained for bare SiO₂NPs. These results are consistent with an increased extent of particle coverage as the number of vesicles per SiO₂NP increases. On the other hand, the hydrodynamic size of M-SiO₂NPs is stable (around 200 nm) in the range 1/50 to 1/5 SiO₂NPs/vesicle ratio, while for higher ratios (i.e., 1/3 and 1/1) the samples display an abrupt increase in the size, reaching very high hydrodynamic diameters (400-600 nm) and polydispersity (around 0.3-0.4). For these dispersions, we observed low colloidal stability, with massive precipitation within 1 h from preparation. This observation can be explained considering that, for high SiO₂NPs/vesicle ratios, the coverage on SiO₂NPs is only partial. In agreement with some recent reports, a lipid surface coverage lower than 40% induces abrupt precipitation¹⁰⁵ due to the presence of membrane patches on the silica surface, triggering the bridging between different -and partially coated- particles^{64,65} (inset in table 1). In the present case, it is reasonable to assume that, for colloidally unstable samples, the vesicles' amount is too low to completely coat the available SiO₂ surface, and, therefore, most of the SiO₂NPs will present a discontinuous surface coverage. The lipid edges of

the bilayer patches represent very high-energy spots, which promote interaction with other uncompleted bilayer shells, inducing particle bridging, and precipitation. In this hypothesis, the dispersions' stability, only achieved for lower SiO₂NPs/vesicle ratios (<1/3), can be considered an indirect proof of the formation of intact bilayer shells around the surface of a significant fraction of the SiO₂NPs.

We then investigated the interaction of AuNPs with M-SiO₂NPs presenting different coating degrees through UV-vis spectroscopy (Figure 3a). For this purpose, the M-SiO₂NPs were incubated with AuNPs under the same experimental conditions described in section 2.2. The incubation provokes a gradual color variation of the original AuNPs dispersion (see Figure 3a inset), from a ruby red to different shades of purple; this is associated with a broadening of the plasmonic primary signal and the appearance of a red-shifted shoulder, previously also observed for the 1/50 SiO₂NPs/vesicles sample (section 2.2). Interestingly, the extent of such variations (especially in terms of the intensity of the red-shifted shoulder) depends on the fraction of membrane-covered SiO₂NPs surface. Specifically, the red-shifted shoulder gets gradually more pronounced with increasing membrane coverage.

To characterize the structure of the AuNP aggregates, we performed Synchrotron Small Angle X-Ray Scattering (SAXS) measurements (Elettra, Trieste, Italy). Figure 3b displays the SAXS profiles obtained for the bare AuNPs and M-SiO₂NPs/AuNPs adducts. The scattering signal arises from a form factor $P(q)$, which accounts for the shape and size of the dispersed objects, and from a structure factor $S(q)$, which depends on interparticle interactions. In our experimental conditions, considering the much higher concentration of the AuNPs, the SiO₂NPs contribution to the

scattering profiles can be regarded as negligible (see Figure S12 in section S4.4). Therefore, the SAXS profiles shown in Figure 3b are only due to the combination of the $P(q)$ and the $S(q)$ of AuNPs, providing specific information on their structure and aggregation extent. In particular, in the low- q range ($0.082 < \text{nm}^{-1} < 0.161$), we notice a power-law dependence between the scattering intensity and q , highlighted by a linear trend in a double-log representation of the profiles. For low scattering vectors values, the scattering signal accounts for the morphology of particles and aggregates. According to the Porod approximation¹⁰⁶, this dependence can be related to the mass fractal dimension of the probed objects, which accounts for the dimensionality of the AuNPs clusters. Specifically, the absolute values of the slopes of the log-log plots can be associated with a Porod coefficient which represents the fractal dimension of the aggregates. The evaluated slope decreases from -0.53 to -1.44 as the membrane coverage increases, as reported in the inset of Figure 3b. In a model-free fashion, such a slope evolution suggests that the aggregation of AuNPs creates larger and more densely packed clusters with increasing SiO₂NPs coverage. Overall, the structural information gained from the SAXS profiles strongly agrees with the plasmonic variations monitored in the UV-Vis spectra.

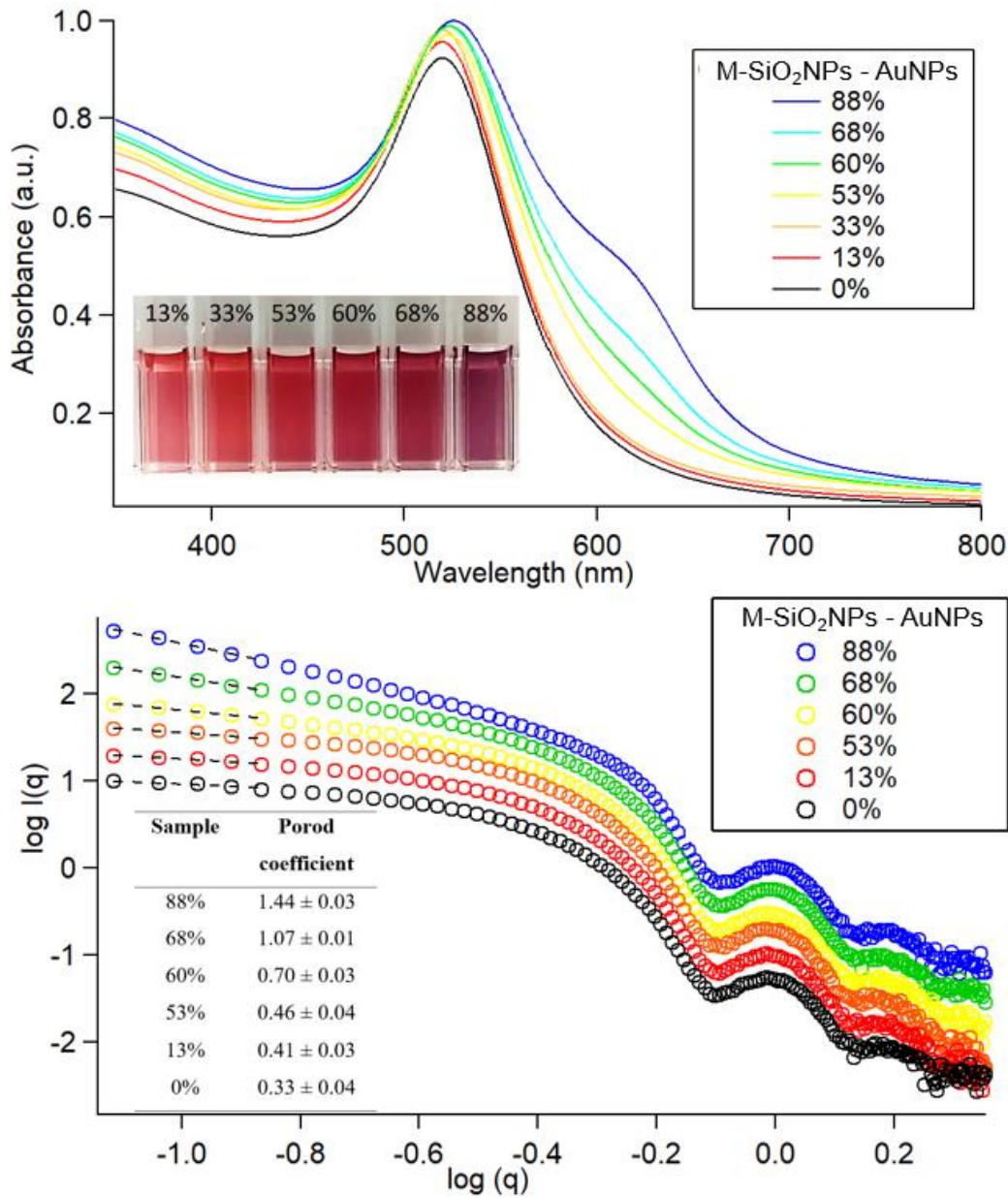


Figure 3. (Top) UV–visible spectra of 6.13 nM AuNPs interacting with 1.15 nM M-SiO₂NPs with different degrees of coverage, collected after 10 min of incubation; (bottom) SAXS profiles of M-SiO₂NPs -AuNPs mixtures with varying degrees of SiO₂NPs membrane coverage collected after 10 minutes of incubation. The inset displays the Porod coefficients extracted from the linear fits (dashed black lines) of the double log plots.

The results from SAXS and UV-Vis show that AuNPs clustering on M-SiO₂NPs is spontaneous and strictly modulated by the coated surface fraction of SiO₂NPs. The plasmonic properties of AuNPs conveniently monitor such dependence through both color and spectral variations of the AuNPs/M-SiO₂NPs dispersion. It is then possible to infer the coating degree from a colorimetric assay by introducing a quantitative descriptor of the plasmonic variations of the AuNPs dispersion. To this aim, we selected an optical index recently used to quantify the variation of optical properties of AuNPs dispersions in the presence of synthetic free-standing vesicles⁹². This aggregation index (A.I.) is calculated by dividing the area subtended by the absorbance spectrum in the 560–800 nm range by the total spectral range area (350–800 nm). The results are then normalized for the A.I. of neat AuNPs, so that the A.I. of neat AuNPs' dispersion is equal to 1 and, increasing the particle aggregation, the A.I. value increases. Table 2 summarizes the A.I.s for each M-SiO₂NPs/AuNPs sample, where the coating degrees vary.

SiO₂NPs coverage	A.I.
88%	1.81 ± 0.05
68%	1.63 ± 0.04
60%	1.45 ± 0.03
53%	1.35 ± 0.02
33%	1.14 ± 0.01
13%	1.07 ± 0.02
0%	1

Table 2. A.I. values obtained for each different membrane coverage of SiO₂NPs.

Figure 4 shows the so-determined A.I. values plotted *versus* the membrane coverage % of SiO₂NPs (inferred quantitatively by ICP-AES). While the gradual color variation of AuNPs (bottom inset in Figure 4) can already provide some qualitative hints on the degree of membrane coverage, the A.I. and the coverage extent of SiO₂NPs are linked by a precise functional relation, which paves the way for developing a spectrophotometric assay for the quantitative determination of membrane coverage. Specifically, the A.I. increases linearly with membrane coverage (r-squared 0.98) over a wide range of coating yields (35-90%). The fitting accuracy decreases when SiO₂NPs with a coverage <35% are included in the linear regression, yielding an r-squared of 0.95 (see section 5.2 of SI). This is probably due to the poor colloidal stability of the M-SiO₂NPs in low coverage conditions, leading to uncontrolled precipitation of M-SiO₂NPs/AuNPs complexes (see Fig. S14 of SI for the correlation between the hydrodynamic size of M-SiO₂NPs and the optical response of AuNPs).

While several qualitative methods (e.g., colloidal stability tests⁶⁸, and sodium dodecyl sulfate-polyacrylamide gel electrophoresis⁷⁵) can easily detect a very poor (<35%) or absent coverage on NPs, this approach offers a precise -and quantitative- determination of membrane integrity at intermediate and/or high membrane coverage levels, which represents the compositional range of interest for the application of NPs in the biomedical field; as a matter of fact, most of the membrane-related surface functionalities of NPs vanish at low coverages⁶⁹⁻⁷¹, while only higher levels of coverage ensure colloidal stability^{63,65} of NPs and partial (or complete) preservation of the biological functions⁶⁸ of their membrane shell.

Moreover, it is worth noticing that since the aggregation of AuNPs is induced by the presence of the lipid bilayer coating, the assay does not depend on the chemical nature of the nanoparticles' inorganic core and could be extended to NPs with different compositions and physicochemical features.

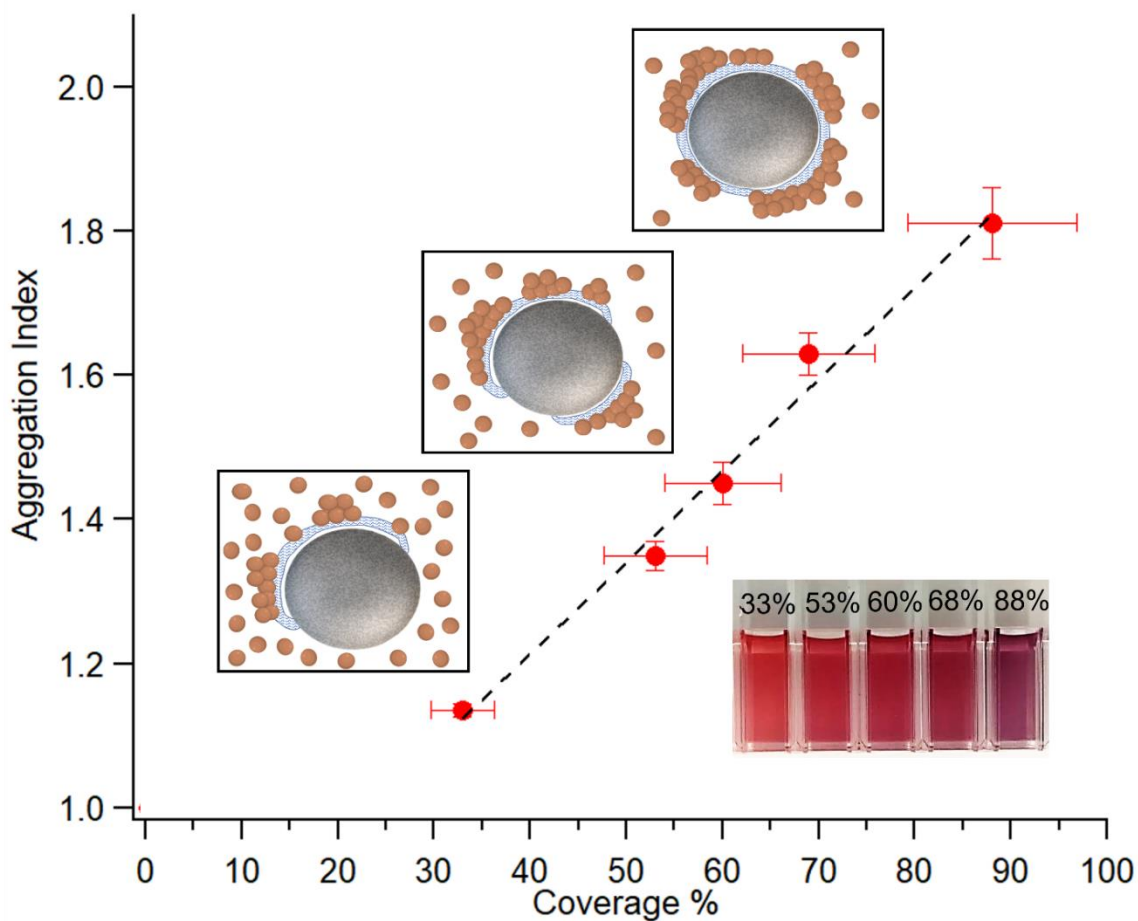


Figure 4. A.I. as a function of SiO₂NPs membrane coverage, with sketches of AuNPs/M-SiO₂ hybrids highlighting how the integrity of the membrane coating affects AuNPs binding and aggregation. Inset: visual appearance of AuNPs incubated with SiO₂NPs at different membrane coverages.

4. Conclusions

In the last years, the production of lipid bilayer-coated materials has proved a powerful approach to increase the biocompatibility of inorganic NPs, reduce adverse side effects, and improve their efficiency. To reach this overarching goal, high-fidelity structural control and the availability of analytical methods amenable to scale-up production are critical. Here we described a straightforward and quantitative assay for determining the extent of biomimetic lipid bilayer coverage on inorganic nanoparticles. Based on previous works, we leveraged the plasmonic properties of Turkevich-Frens AuNPs and their sensitivity to the AuNP aggregation extent to develop an effective method for the quantification of lipid membrane coating on inorganic NPs. By challenging SiO₂NPs of different -and known- lipid coverage degrees with AuNPs, we show that, in the region of colloidal stability, the plasmonic descriptor of AuNPs' optical properties linearly varies with the amount of lipid coverage and that this dependence can be leveraged for estimating the coverage extent. As a difference from the already available methods^{72-74,79-81}, such assay provides a fast and high-throughput readout of membrane integrity at an ensemble-averaged level, which only requires cheap reagents, standard lab instrumentation, and limited users experience. From a different -but equally important- perspective, we also showed that a lipid membrane could drive and control the self-assembly of AuNPs on an inorganic nanosized scaffold, which enables the possibility of creating complex hybrid materials composed of an inorganic core, a lipid bilayer shell and a further plasmonic shell of tuneable optical properties. The easiness of preparation, which exploits the spontaneous self-assembly of AuNPs, can inspire the production

of multicomponent biocompatible nanomaterials with high structural fidelity and mild experimental conditions.

Authors information

Corresponding Author

Debora Berti (Department of Chemistry “Ugo Schiff”, University of Florence, Florence, Italy and CSGI, Consorzio Sistemi a Grande Interfase, University of Florence, Sesto Fiorentino, Italy, email: debora.berti@unifi.it); Lucrezia Caselli (Department of Physical Chemistry 1, University of Lund, SE-22100 Lund, Sweden, email: lucrezia.caselli@fkem1.lu.se)

Funding Sources

This work has been supported by the European Community through the BOW project (H2020-EIC-FETPROACT2019, ID 952183). We also acknowledge MIUR-Italy (“Progetto Dipartimenti di Eccellenza 2018–2022, ref B96C1700020008” allocated to the Department of Chemistry “Ugo Schiff”) and Ente Cassa di Risparmio di Firenze for economic support.

Acknowledgements

Prof. Paolo Arosio and Karl Normak (Biochemical Engineering Laboratory, ETH Zurich, Switzerland) are acknowledged for sharing their knowledge on the membrane composition and preparation of the liposomal models for EVs employed herein, as well as for fruitful discussion on the design of M-SiO₂NPs. The Elettra Synchrotron SAXS facility (Basovizza, Trieste, Italy) is acknowledged for beam time (Proposal id: 20212182). We acknowledge the Florence Center for Electron Nanoscopy (FloCEN) at the University of Florence.

Abbreviations

SiO₂NPs, silica nanoparticles; AuNPs, gold nanoparticles; M-SiO₂NPs, membrane coated silica nanoparticles; EVs, Extracellular Vesicles.

References

- 1 S. Gavas, S. Quazi and T. M. Karpiński, *Nanoscale Res. Lett.*, 2021, **16**, 173.
- 2 S. Hua, M. B. C. de Matos, J. M. Metselaar and G. Storm, *Front. Pharmacol.*, , DOI:10.3389/fphar.2018.00790.
- 3 M. Henriksen-Lacey, S. Carregal-Romero and L. M. Liz-Marzán, *Bioconjug. Chem.*, 2017, **28**, 212–221.
- 4 M. Hofmann-Antenbrink, D. W. Grainger and H. Hofmann, *Nanomedicine Nanotechnology, Biol. Med.*, 2015, **11**, 1689–1694.
- 5 S. Barua and S. Mitragotri, *Nano Today*, 2014, **9**, 223–243.
- 6 E. Pedziwiatr-Werbicka, K. Horodecka, D. Shcharbin and M. Bryszewska, *Curr. Med. Chem.*, 2020, **28**, 346–359.
- 7 N. Zhang, J. Lin and S. Y. Chew, *ACS Appl. Mater. Interfaces*, 2021, **13**, 55840–55850.

- 8 X. Zhen, P. Cheng and K. Pu, *Small*, 2019, **15**, 1–19.
- 9 M. Wu, W. Le, T. Mei, Y. Wang, B. Chen, Z. Liu and C. Xue, *Int. J. Nanomedicine*, 2019, **Volume 14**, 4431–4448.
- 10 R. H. Fang, C. M. J. Hu, B. T. Luk, W. Gao, J. A. Copp, Y. Tai, D. E. O’Connor and L. Zhang, *Nano Lett.*, 2014, **14**, 2181–2188.
- 11 L. Zhang, X. Zhang, G. Lu, F. Li, W. Bao, C. Song, W. Wei and G. Ma, *Small*, 2019, **15**, 1–13.
- 12 M. Zhou, Y. Xing, X. Li, X. Du, T. Xu and X. Zhang, *Small*, 2020, **16**, 1–11.
- 13 M. M. Van Schooneveld, E. Vucic, R. Koole, Y. Zhou, J. Stocks, D. P. Cormode, C. Y. Tang, R. E. Gordon, K. Nicolay, A. Meijerink, Z. A. Fayad and W. J. M. Mulder, *Nano Lett.*, 2008, **8**, 2517–2525.
- 14 A. Luchini and G. Vitiello, *Front. Chem.*, 2019, **7**, 1–16.
- 15 J. Yang, J. Tu, G. E. M. Lamers, R. C. L. Olsthoorn and A. Kros, *Adv. Healthc. Mater.*, 2017, **6**, 1–7.
- 16 K. S. Butler, P. N. Durfee, C. Theron, C. E. Ashley, E. C. Carnes and C. J. Brinker, *Small*,

- 2016, **12**, 2173–2185.
- 17 G. D. Bothun, *J. Nanobiotechnology*, 2008, **6**, 1–10.
- 18 M. Sancho-Albero, M. del M. Encabo-Berzosa, M. Beltrán-Visiedo, L. Fernández-Messina, V. Sebastián, F. Sánchez-Madrid, M. Arruebo, J. Santamaría and P. Martín-Duque, *Nanoscale*, 2019, **11**, 18825–18836.
- 19 M. Sancho-Albero, B. Rubio-Ruiz, A. M. Pérez-López, V. Sebastián, P. Martín-Duque, M. Arruebo, J. Santamaría and A. Unciti-Broceta, *Nat. Catal.*, 2019, **2**, 864–872.
- 20 C.-M. J. Hu, L. Zhang, S. Aryal, C. Cheung, R. H. Fang and L. Zhang, *Proc. Natl. Acad. Sci.*, 2011, **108**, 10980–10985.
- 21 C. Ferrel, S. Rayamajhi, T. Nguyen, R. Marasini, T. Saravanan, F. Deba and S. Aryal, *ACS Appl. Bio Mater.*, 2021, **4**, 6974–6981.
- 22 J. Peng, Q. Yang, W. Li, L. Tan, Y. Xiao, L. Chen, Y. Hao and Z. Qian, *ACS Appl. Mater. Interfaces*, 2017, **9**, 44410–44422.
- 23 Q. Pei, X. Hu, X. Zheng, S. Liu, Y. Li, X. Jing and Z. Xie, *ACS Nano*, 2018, **12**, 1630–1641.

- 24 J. P. Thawani, A. Amirshaghghi, L. Yan, J. M. Stein, J. Liu and A. Tsourkas, *Small*, 2017, **13**, 1–9.
- 25 S. Krishnamurthy, M. K. Gnanasammandhan, C. Xie, K. Huang, M. Y. Cui and J. M. Chan, *Nanoscale*, 2016, **8**, 6981–6985.
- 26 H. Zhao, L. Li, J. Zhang, C. Zheng, K. Ding, H. Xiao, L. Wang and Z. Zhang, *ACS Appl. Mater. Interfaces*, 2018, **10**, 31124–31135.
- 27 L. Rao, Z. He, Q.-F. Meng, Z. Zhou, L.-L. Bu, S.-S. Guo, W. Liu and X.-Z. Zhao, *J. Biomed. Mater. Res. Part A*, 2017, **105**, 521–530.
- 28 Z. Chen, P. Zhao, Z. Luo, M. Zheng, H. Tian, P. Gong, G. Gao, H. Pan, L. Liu, A. Ma, H. Cui, Y. Ma and L. Cai, *ACS Nano*, 2016, **10**, 10049–10057.
- 29 C. Liu, D. Wang, S. Zhang, Y. Cheng, F. Yang, Y. Xing, T. Xu, H. Dong and X. Zhang, *ACS Nano*, 2019, **13**, 4267–4277.
- 30 J.-Y. Zhu, D.-W. Zheng, M.-K. Zhang, W.-Y. Yu, W.-X. Qiu, J.-J. Hu, J. Feng and X.-Z. Zhang, *Nano Lett.*, 2016, **16**, 5895–5901.
- 31 Z. Gao, L. Zhang, J. Hu and Y. Sun, *Nanomedicine Nanotechnology, Biol. Med.*, 2013, **9**, 174–184.

- 32 X. Geng, D. Gao, D. Hu, Q. Liu, C. Liu, Z. Yuan, X. Zhang, X. Liu, Z. Sheng, X. Wang and H. Zheng, *ACS Appl. Mater. Interfaces*, 2020, **12**, 55624–55637.
- 33 Q. Jiang, K. Wang, X. Zhang, B. Ouyang, H. Liu, Z. Pang and W. Yang, *Small*, 2020, **16**, 2001704.
- 34 C.-H. Luo, C.-T. Huang, C.-H. Su and C.-S. Yeh, *Nano Lett.*, 2016, **16**, 3493–3499.
- 35 D. T. Riglar and P. A. Silver, *Nat. Rev. Microbiol.*, 2018, **16**, 214–225.
- 36 V. Gujrati, S. Kim, S.-H. Kim, J. J. Min, H. E. Choy, S. C. Kim and S. Jon, *ACS Nano*, 2014, **8**, 1525–1537.
- 37 T. Kang, Q. Zhu, D. Wei, J. Feng, J. Yao, T. Jiang, Q. Song, X. Wei, H. Chen, X. Gao and J. Chen, *ACS Nano*, 2017, **11**, 1397–1411.
- 38 Y. Fu, G. He, Z. Liu, J. Wang, M. Li, Z. Zhang, Q. Bao, J. Wen, X. Zhu, C. Zhang and W. Zhang, 2022, **2202337**, 1–11.
- 39 M. Wu, X. Liu, H. Bai, L. Lai, Q. Chen, G. Huang, B. Liu and G. Tang, *ACS Appl. Mater. Interfaces*, 2019, **11**, 9850–9859.
- 40 J. Li, X. Zhen, Y. Lyu, Y. Jiang, J. Huang and K. Pu, *ACS Nano*, 2018, **12**, 8520–8530.

- 41 L. Rao, B. Cai, L.-L. Bu, Q.-Q. Liao, S.-S. Guo, X.-Z. Zhao, W.-F. Dong and W. Liu, *ACS Nano*, 2017, **11**, 3496–3505.
- 42 X. Zhen, P. Cheng and K. Pu, *Small*, 2019, **15**, 1804105.
- 43 L. Zhu, Y. Zhong, S. Wu, M. Yan, Y. Cao, N. Mou, G. Wang, D. Sun and W. Wu, *Mater. Today Bio*, 2022, **14**, 100228.
- 44 D. Wang, C. Liu, S. You, K. Zhang, M. Li, Y. Cao, C. Wang, H. Dong and X. Zhang, *ACS Appl. Mater. Interfaces*, 2020, **12**, 41138–41147.
- 45 J. R. Fitzgerald, T. J. Foster and D. Cox, *Nat. Rev. Microbiol.*, 2006, **4**, 445–457.
- 46 C.-M. J. Hu, R. H. Fang, J. Copp, B. T. Luk and L. Zhang, *Nat. Nanotechnol.*, 2013, **8**, 336–340.
- 47 Q. Zhang, D. Dehaini, Y. Zhang, J. Zhou, X. Chen, L. Zhang, R. H. Fang, W. Gao and L. Zhang, *Nat. Nanotechnol.*, 2018, **13**, 1182–1190.
- 48 R. H. Fang, C.-M. J. Hu, B. T. Luk, W. Gao, J. A. Copp, Y. Tai, D. E. O’Connor and L. Zhang, *Nano Lett.*, 2014, **14**, 2181–2188.
- 49 H.-W. Chen, Z.-S. Fang, Y.-T. Chen, Y.-I. Chen, B.-Y. Yao, J.-Y. Cheng, C.-Y. Chien, Y.-

- C. Chang and C.-M. J. Hu, *ACS Appl. Mater. Interfaces*, 2017, **9**, 39953–39961.
- 50 P. Fathi, L. Rao and X. Chen, *View*, 2021, **2**, 20200187.
- 51 R. Van Der Meel, M. H. A. M. Fens, P. Vader, W. W. Van Solinge, O. Eniola-Adefeso and R. M. Schiffelers, *J. Control. Release*, 2014, **195**, 72–85.
- 52 G. Raposo and W. Stoorvogel, *J. Cell Biol.*, 2013, **200**, 373–383.
- 53 H. Saari, E. Lázaro-Ibáñez, T. Viitala, E. Vuorimaa-Laukkanen, P. Siljander and M. Yliperttula, *J. Control. Release*, 2015, **220**, 727–737.
- 54 S. Busatto, A. Giacomini, C. Montis, R. Ronca and P. Bergese, *Anal. Chem.*, 2018, **90**, 7855–7861.
- 55 S. Kamerkar, V. S. LeBleu, H. Sugimoto, S. Yang, C. F. Ruivo, S. A. Melo, J. J. Lee and R. Kalluri, *Nature*, 2017, **546**, 498–503.
- 56 S. EL Andaloussi, I. Mäger, X. O. Breakefield and M. J. A. Wood, *Nat. Rev. Drug Discov.*, 2013, **12**, 347–357.
- 57 S. EL Andaloussi, S. Lakhal, I. Mäger and M. J. A. Wood, *Adv. Drug Deliv. Rev.*, 2013, **65**, 391–397.

- 58 M. J. Haney, N. L. Klyachko, Y. Zhao, R. Gupta, E. G. Plotnikova, Z. He, T. Patel, A. Piroyan, M. Sokolsky, A. V. Kabanov and E. V. Batrakova, *J. Control. Release*, 2015, **207**, 18–30.
- 59 O. M. Elsharkasy, J. Z. Nordin, D. W. Hagey, O. G. de Jong, R. M. Schiffelers, S. EL Andaloussi and P. Vader, *Adv. Drug Deliv. Rev.*, 2020, **159**, 332–343.
- 60 C. Liu, W. Zhang, Y. Li, J. Chang, F. Tian, F. Zhao, Y. Ma and J. Sun, *Nano Lett.*, 2019, **19**, 7836–7844.
- 61 G. Cheng, W. Li, L. Ha, X. Han, S. Hao, Y. Wan, Z. Wang, F. Dong, X. Zou, Y. Mao and S.-Y. Zheng, *J. Am. Chem. Soc.*, 2018, **140**, 7282–7291.
- 62 J. Wang, Y. Dong, Y. Li, W. Li, K. Cheng, Y. Qian, G. Xu, X. Zhang, L. Hu, P. Chen, W. Du, X. Feng, Y. Di Zhao, Z. Zhang and B. F. Liu, *Adv. Funct. Mater.*, 2018, **28**, 1–14.
- 63 A. H. Bahrami, M. Raatz, J. Agudo-canalejo, R. Michel, E. M. Curtis, C. K. Hall, M. Gradzielski, R. Lipowsky, T. R. Weikl, M. Raphael, C. E. M, H. C. K, G. Michael and L. Rein-, *Adv. Colloid Interface Sci.*, , DOI:10.1016/j.cis.2014.02.012.
- 64 R. Michel and M. Gradzielski, *Int. J. Mol. Sci.*, 2012, **13**, 11610–11642.
- 65 S. Mornet, O. Lambert, E. Duguet and A. Brisson, *Nano Lett.*, 2005, **5**, 281–285.

- 66 J. Liu, X. Jiang, C. Ashley and C. J. Brinker, *J. Am. Chem. Soc.*, 2009, **131**, 7567–7569.
- 67 J. Van Deun, Q. Roux, S. Deville, T. Van Acker, P. Rappu, I. Miinalainen, J. Heino, F. Vanhaecke, B. G. De Geest, O. De Wever and A. Hendrix, *Cells*, 2020, **9**, 1797.
- 68 L. Liu, X. Bai, M.-V. Martikainen, A. Kårlund, M. Roponen, W. Xu, G. Hu, E. Tasciotti and V.-P. Lehto, *Nat. Commun.*, 2021, **12**, 5726.
- 69 M. Hadjidemetriou, Z. Al-Ahmady, M. Mazza, R. F. Collins, K. Dawson and K. Kostarelos, *ACS Nano*, 2015, **9**, 8142–8156.
- 70 F. Persson, J. Fritzsche, K. U. Mir, M. Modesti, F. Westerlund and J. O. Tegenfeldt, *Nano Lett.*, 2012, **12**, 2260–2265.
- 71 R. C. Van Lehn, M. Ricci, P. H. J. Silva, P. Andreozzi, J. Reguera, K. Voitchovsky, F. Stellacci and A. Alexander-Katz, *Nat. Commun.*, 2014, **5**, 4482.
- 72 A. E. LaBauve, T. E. Rinker, A. Nouredine, R. E. Serda, J. Y. Howe, M. B. Sherman, A. Rasley, C. J. Brinker, D. Y. Sasaki and O. A. Negrete, *Sci. Rep.*, 2018, **8**, 13990.
- 73 D. B. Tada, E. Suraniti, L. M. Rossi, C. A. P. Leite, C. S. Oliveira, T. C. Tumolo, R. Calemczuk, T. Livache and M. S. Baptista, *J. Biomed. Nanotechnol.*, 2014, **10**, 519–528.

- 74 C. Gao, Q. Huang, C. Liu, C. H. T. Kwong, L. Yue, J.-B. Wan, S. M. Y. Lee and R. Wang, *Nat. Commun.*, 2020, **11**, 2622.
- 75 W. Liu, M. Zou, T. Liu, J. Zeng, X. Li, W. Yu, C. Li, J. Ye, W. Song, J. Feng and X. Zhang, *Nat. Commun.*, 1–12.
- 76 L. Zhang, Y. Zhu, X. Wei, X. Chen, Y. Li, Y. Zhu, J. Xia, Y. Huang, Y. Huang, J. Wang and Z. Pang, *Acta Pharm. Sin. B*, 2022, **12**, 3427–3447.
- 77 J. Zhuang, H. Gong, J. Zhou, Q. Zhang and W. Gao, .
- 78 W. Liu, M. Zou, T. Liu, J. Zeng, X. Li, W. Yu and C. Li, 2019, **1900499**, 1–10.
- 79 L. P. Arnett, M. W. Forbes, R. Keunen and M. A. Winnik, *Langmuir*, 2021, **37**, 14605–14613.
- 80 J. Y. Lee, H. Wang, G. Pyrgiotakis, G. M. DeLoid, Z. Zhang, J. Beltran-Huarac, P. Demokritou and W. Zhong, *Anal. Bioanal. Chem.*, 2018, **410**, 6155–6164.
- 81 X. Zhang, A. K. Pandiakumar, R. J. Hamers and C. J. Murphy, , DOI:10.1021/acs.analchem.8b03911.
- 82 R. Kariuki, R. Penman, S. J. Bryant, R. Orrell-Trigg, N. Meftahi, R. J. Crawford, C. F.

- McConville, G. Bryant, K. Voitchovsky, C. E. Conn, A. J. Christofferson and A. Elbourne, *ACS Nano*, 2022, **16**, 17179–17196.
- 83 K. Sugikawa, T. Kadota, K. Yasuhara and A. Ikeda, *Angew. Chemie - Int. Ed.*, 2016, **55**, 4059–4063.
- 84 F. Wang and J. Liu, *Nanoscale*, 2015, **7**, 15599–15604.
- 85 F. Wang, D. E. Curry and J. Liu, *Langmuir*, 2015, **31**, 13271–13274.
- 86 C. Montis, D. Maiolo, I. Alessandri, P. Bergese and D. Berti, *Nanoscale*, 2014, **6**, 6452–6457.
- 87 S. Salassi, L. Caselli, J. Cardellini, E. Lavagna, C. Montis, D. Berti and G. Rossi, *J. Chem. Theory Comput.*, 2021, **17**, 6597–6609.
- 88 J. Cardellini, C. Montis, F. Barbero, I. De Santis, L. Caselli and D. Berti, *Front. Bioeng. Biotechnol.*, , DOI:10.3389/fbioe.2022.848687.
- 89 A. Ridolfi, L. Caselli, C. Montis, G. Mangiapia, D. Berti, M. Brucale and F. Valle, *J. Microsc.*, 2020, **280**, 194–203.
- 90 C. Montis, L. Caselli, F. Valle, A. Zandrini, F. Carlà, R. Schweins, M. Maccarini, P. Bergese

- and D. Berti, *J. Colloid Interface Sci.*, 2020, **573**, 204–214.
- 91 J. Cardellini, L. Caselli, E. Lavagna, S. Salassi, H. Amenitsch, M. Calamai, C. Montis, G. Rossi and D. Berti, *J. Phys. Chem. C*, 2022, **126**, 4483–4494.
- 92 L. Caselli, A. Ridolfi, J. Cardellini, L. Sharpnack, L. Paolini, M. Brucale, F. Valle, C. Montis, P. Bergese and D. Berti, *Nanoscale Horizons*, 2021, **6**, 543–550.
- 93 D. Maiolo, L. Paolini, G. Di Noto, A. Zandrini, D. Berti, P. Bergese and D. Ricotta, *Anal. Chem.*, 2015, **87**, 4168–4176.
- 94 J. Turkevich, P. C. Stevenson and J. Hillier, *Discuss. Faraday Soc.*, 1951, **11**, 55–75.
- 95 G. Frens, *Nat. Phys. Sci.*, 1973, **241**, 20–22.
- 96 J. L. Hutter and J. Bechhoefer, *Rev. Sci. Instrum.*, 1993, **64**, 1868–1873.
- 97 D. J. Müller, D. Fotiadis, S. Scheuring, S. A. Müller and A. Engel, *Biophys. J.*, 1999, **76**, 1101–1111.
- 98 J. G. Croissant, K. S. Butler, J. I. Zink and C. J. Brinker, *Nat. Rev. Mater.*, 2020, **5**, 886–909.

- 99 A. Watermann and J. Brieger, *Nanomaterials*, , DOI:10.3390/nano7070189.
- 100 A. Llorente, T. Skotland, T. Sylvänne, D. Kauhanen, T. Róg, A. Orłowski, I. Vattulainen, K. Ekroos and K. Sandvig, *Biochim. Biophys. Acta - Mol. Cell Biol. Lipids*, 2013, **1831**, 1302–1309.
- 101 P. J. Chung, H. L. Hwang, K. Dasbiswas, A. Leong and K. Y. C. Lee, *Langmuir*, 2018, **34**, 13000–13005.
- 102 P. A. Hassan, S. Rana and G. Verma, *Langmuir*, 2015, **31**, 3–12.
- 103 M. Kaasalainen, V. Aseyev, E. von Haartman, D. Ş. Karaman, E. Mäkilä, H. Tenhu, J. Rosenholm and J. Salonen, *Nanoscale Res. Lett.*, 2017, **12**, 74.
- 104 A. Zandrini, L. Paolini, S. Busatto, A. Radeghieri, M. Romano, M. H. M. Wauben, M. J. C. van Herwijnen, P. Nejsun, A. Borup, A. Ridolfi, C. Montis and P. Bergese, *Front. Bioeng. Biotechnol.*, 2020, **7**, 1–10.
- 105 S. Savarala, F. Monson, M. A. Ilies and S. L. Wunder, *Langmuir*, 2011, **27**, 5850–5861.
- 106 L. A. Feigin and D. I. Svergun, *Structure Analysis by Small-Angle X-Ray and Neutron Scattering*, Springer US, Boston, MA, 1987.

Supporting Information

Probing the coverage of nanoparticles by biomimetic membranes through nanoplasmonics

Jacopo Cardellini^{1,2}, Andrea Ridolfi^{1,2,3,4}, Melissa Donati¹, Valentina Giampietro¹, Mirko Severi¹, Marco Brucale^{2,3}, Francesco Valle^{2,3}, Paolo Bergese^{2,5,6}, Costanza Montis^{1,2}, Lucrezia Caselli^{1,2,7}, and Debora Berti^{1,2*}*

1 Department of Chemistry “Ugo Schiff”, University of Florence, Florence, Italy

2 CSGI, Consorzio Sistemi a Grande Interfase, University of Florence, Sesto Fiorentino, Italy

3 Istituto per lo Studio dei Materiali Nanostrutturati, Consiglio Nazionale delle Ricerche, 40129 Bologna, Italy

4 Department of Physics and Astronomy and LaserLaB Amsterdam, Vrije Universiteit Amsterdam, Amsterdam, The Netherlands (current affiliation)

5 Department of Molecular and Translational Medicine, University of Brescia, Brescia, Italy

6 Consorzio Interuniversitario Nazionale per la Scienza e la Tecnologia dei Materiali, Florence, Italy

7 Department of Pharmacy, University of Copenhagen, DK-2100 Copenhagen, Denmark (current affiliation)

*E-mails: debora.berti@unifi.it, lucrezia.caselli@fkem1.lu.se (corresponding authors)

Keywords: lipid-coated nanoparticles, gold nanoparticles, nanoplasmonics, biomimetic nanoparticles, silica nanoparticles, nano-bio interface, Extracellular Vesicles membrane

1 Supplementary Characterization of Liposomes	
1.1 Dynamic Light Scattering and Z-Potential	
1.2 Evaluation of liposomes concentration	
2 Supplementary Characterization of Coated SiNPs	
2.1 Cryo-TEM	
2.2 Atomic Force microscopy	
2.3 Evaluation of the degree of coverage	
3 Supplementary Characterization of AuNPs	
3.1 Small Angle X-ray Scattering	
3.2 Dynamic Light Scattering	
3.3 UV-vis spectroscopy	
4 Supplementary Characterization of Coated SiNPs/AuNPs hybrids	
4.1 Cryo-TEM	
4.2 Dynamic Light Scattering	
4.3 UV-vis spectroscopy	
4.4 Small Angle X-ray Scattering	
5 Supplementary Characterization of Coated SiNPs with different coverage	
5.1 Dynamic Light Scattering	
5.2 Nanoplasmonic assay for the quantification of the SiNPs lipid coverage	

1 Supplementary Characterization of Liposomes

1.1 Dynamic Light Scattering and Z-Potential

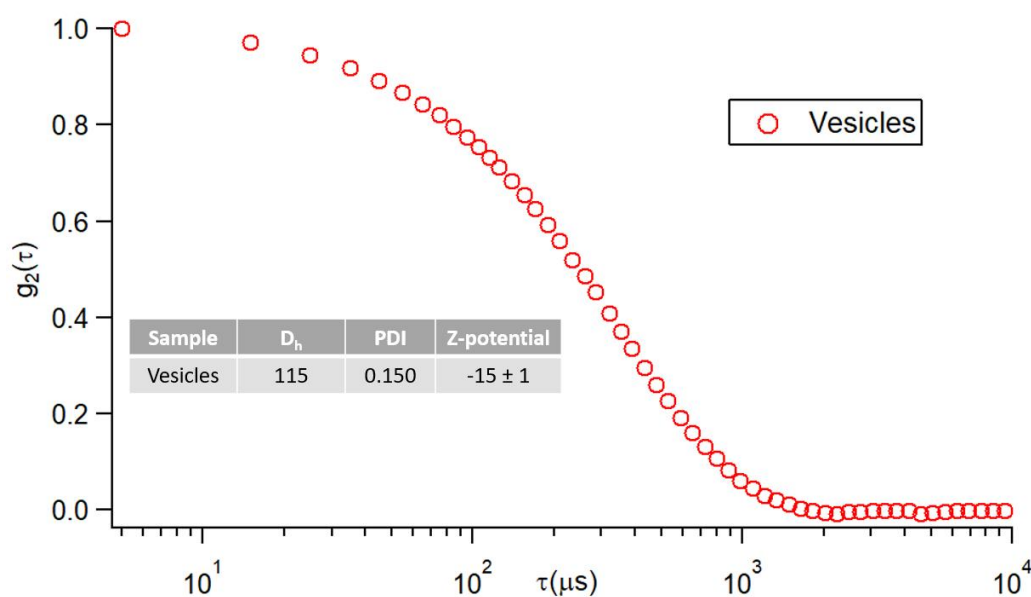


Fig S1: Autocorrelation function collected for the vesicles' dispersion at a concentration of 0.35 mg/mL. The table in the inset shows the hydrodynamic diameter and the polydispersity index (PDI), evaluated with the cumulant analysis, and the surface ζ -potential.

1.2 Evaluation of Liposomes concentration

The lipid concentration in the starting colloidal dispersion was estimated to be 7 mg/mL from the initial lipid and water amounts employed in the formation and swelling of lipid films, assuming the absence of lipid loss due to the extrusion procedure. The liposomes concentration in the final dispersion was subsequently calculated considering their hydrodynamic diameter (Fig. S1). In particular, the liposomal surface area (surface area= $4\pi r^2$) can be extracted from the liposome diameters; the doubled surface can be subsequently divided by the lipid cross section

(approximately 0.5 nm^2) in order to obtain the lipid number per liposome, assuming that approximately one half of the lipids is localized in the external leaflet of a liposome, since the bilayer thickness, about 4-5 nm, is negligible with respect to the liposomes' average diameter. Eventually, the total weighted lipid concentration was divided by the total number of lipids per liposome. A liposome concentration of 7.998×10^{13} vesicles/mL was obtained, corresponding to a molar concentration of $13 \times 10^{-8} \text{ M}$. The liposomal dispersions were diluted to reach a final concentration of $5 \cdot 10^{13}$ vesicles/mL before use (corresponding to a molar concentration of $9.5 \times 10^{-8} \text{ M}$).

2 Supplementary Characterization of M-SiO₂NPs

2.1 Cryo-TEM

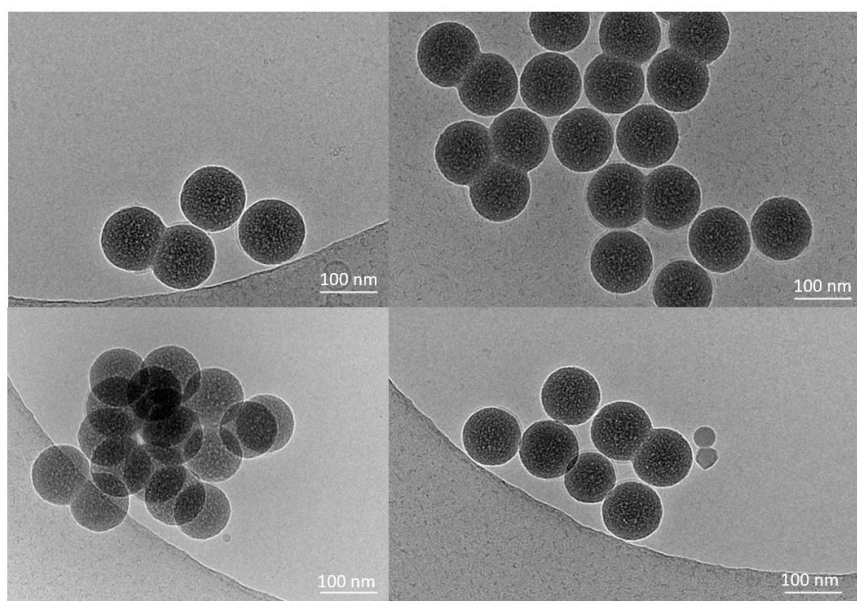


Fig S2: Cryo-TEM images of SiO₂NPs with a membrane coverage of 88%.

2.2 Atomic Force Microscopy

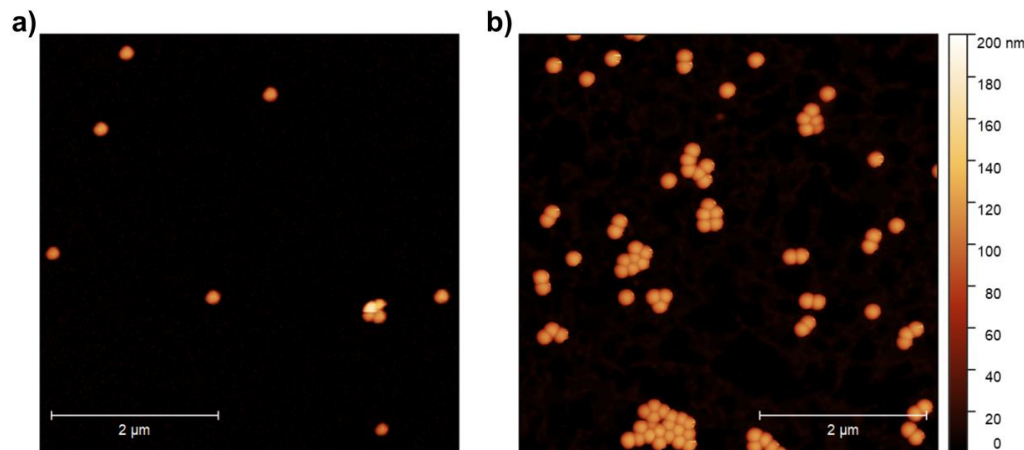


Fig S3: Representative AFM images of a) SiO₂NPs and b) M-SiO₂NPs.

2.3 Evaluation of the degree of coverage

To evaluate the degree of lipid coverage of each sample, we performed ICP-AES measurements. With this method we were able to determine (in terms of mg per liters) the amount of P and Si within the dispersion. The obtained values were reported in table S1. Starting from such values we evaluated the lipid coverage of SiO₂NPs for each formulation, according to the following procedure. The amount of P was used for calculating the moles of lipids in the samples. Considering AFM results, the size of M-SiO₂NPs is approximately 140 nm. Thus, the amount of lipids needed for the formation of a lipid bilayer around a single SiO₂NP can be approximated to be equal to the amount of lipid composing a liposome of 140 nm in diameter (following the procedure reported in section S1.2).

For evaluating the concentration of SiO₂NPs in each sample after 6 cycles of centrifugation, the total mass of SiO₂NPs was obtained starting from the amount of Si measured by the ICP-MS analysis. Then, the mass of a single SiO₂NP was obtained from the density of the SiO₂NP ($d=1.9 \text{ g/cm}^3$) and the volume of a single SiO₂NP of 120 nm in diameter (904320 nm^3). The number of SiO₂NPs present in the sample was obtained by dividing the total mass of SiO₂NPs for the mass of a single SiO₂NP. Finally, to obtain the percentage of covered SiO₂NP surface, the total number of lipids (calculated from ICP-AES data as described above) was divided by the number of lipids theoretically needed for fully covering the number of SiO₂NPs present in the sample.

The obtained results are reported in table S3. Each sample was diluted to a SiO₂ concentration of 1.15 nM before each further measurement.

Sample	P mg/L	Si mg/L	SiNPs coverage
50/1	8.9 ± 0.8	596.3	88 ± 8 %
15/1	7.2 ± 0.7	626.3	68 ± 7 %
10/1	5.9 ± 0.6	579.0	60 ± 6 %
5/1	5.0 ± 0.5	557.4	53 ± 5 %
3/1	3.2 ± 0.3	570.9	33 ± 3 %
1/1	1.0 ± 0.1	462.3	13 ± 1%

Table S1: mg/L concentration of the samples obtained by ICP-AES measurements.

3 Supplementary Characterization of Gold Nanoparticles

3.1 Small Angle X-ray Scattering

SAXS measurements on AuNPs aqueous dispersion were carried out in sealed glass capillaries of 1.5 mm diameter.

The structural parameters (Table S2) of citrate-coated gold nanoparticles were evaluated from the SAXS profile of their diluted water dispersion (2.06 n M) (Figure S1), according to a spherical form factor and a Schulz size distribution. In our concentration range, we can safely assume that there are no interparticle interactions, and that the structure factor $S(Q)$ is equal to 1 in the whole range of scattering vectors. Thus, the scattering profile of the particles derives from their form factor, $P(Q)$. The SAXS spectrum reported in Figure S1 is fully consistent with the characteristic $P(Q)$ of spherical particles with an average diameter of about 5.8 nm. The clear presence of $P(Q)$ oscillations in the high Q region is consistent with a relatively low polydispersity of the synthesized AuNPs.

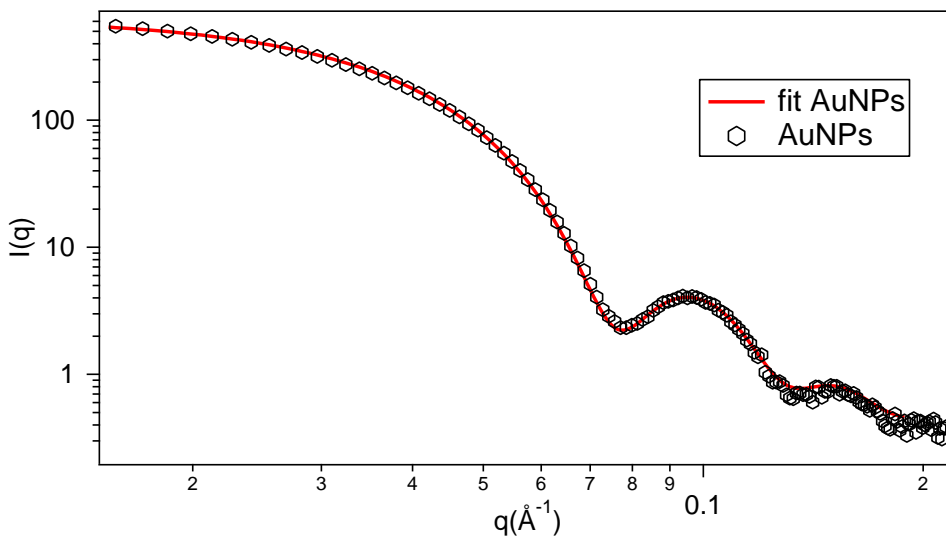


Figure S4: Experimental SAXS curve (red markers) obtained for AuNPs, and curve fit (solid black line) according to the Schulz spheres model from the analysis software package SasView. The size and polydispersity obtained from the fitting procedure are summarized in the Table S1 below.

	R_{core} (nm)	poly
AuNP	5.8	0.095

Table S2: Structural parameters of the nanoparticles obtained from the analysis of SAXS curves according to the Schulz spheres model.

3.2 Dynamic Light Scattering and ζ -Potential

AuNPs hydrodynamic diameter and surface charge in MilliQ water were evaluated through Dynamic Light Scattering and ζ -Potential, respectively, and reported in inset of figure S5.

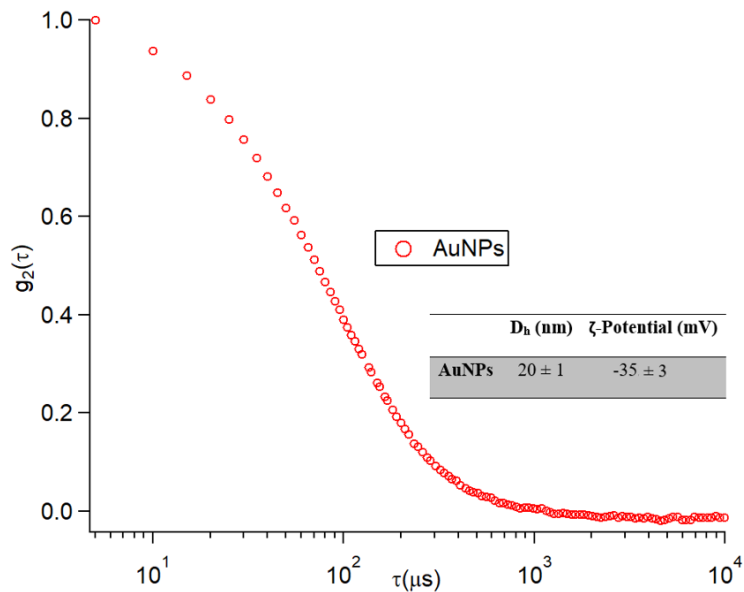


Figure S5: Hydrodynamic diameter obtained from Dynamic Light Scattering and surface ζ -Potential of AuNPs.

3.3 UV-vis Spectroscopy

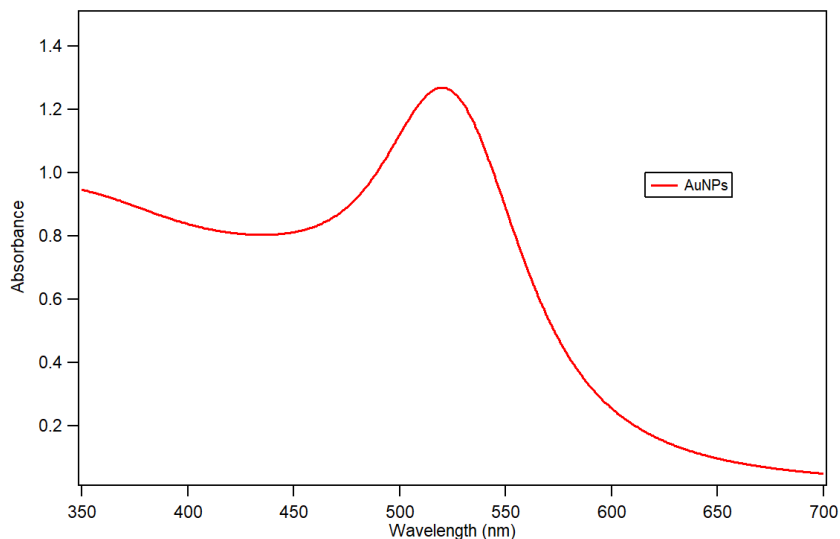


Figure S6 UV-Vis absorption spectra of AuNPs after 1:3 dilution in water (2.06 nm). The plasmon absorption peak is at around 520 nm.

To further evaluate the AuNPs size through UV-Vis spectroscopy we exploited the following equation¹:

$$d = \exp \left(B_1 \frac{A_{spr}}{A_{450}} - B_2 \right)$$

with d diameter of gold nanoparticles, A_{spr} absorbance at the surface plasma resonance peak, A_{450} absorbance at the wavelength of 450 nm and B_1 and B_2 are dimensionless parameters, taken as 3 and 2.2, respectively. The diameter value obtained is of 12.3 nm.

The concentration of citrate-coated gold nanoparticles was determined via UV-Vis spectrometry, using the Lambert-Beer law ($E(\lambda) = \varepsilon(\lambda)lc$), taking the extinction values $E(\lambda)$ at the LSPR maximum, i.e. $\lambda = 521$ nm. The extinction coefficient $\varepsilon(\lambda)$ of gold nanoparticles dispersion was determined by the method reported in literature², by the following equation:

$$\ln(\varepsilon) = k \ln(d) + a$$

with d core diameter of nanoparticles, and k and a dimensionless parameters ($k = 3,32111$ and $a = 10,80505$). The arithmetic mean of the sizes obtained by optical and scattering analyses was selected, leading to a $\varepsilon(\lambda)$ of $2.0 \cdot 10^8 \text{ m}^{-1} \text{ cm}^{-1}$. The final concentration of the citrate-coated AuNPs is therefore $\sim 6.13 \cdot 10^{-9} \text{ M}$.

4 Supplementary Characterization of M-SiO₂NPs/AuNPs hybrids

4.1 Cryo-TEM

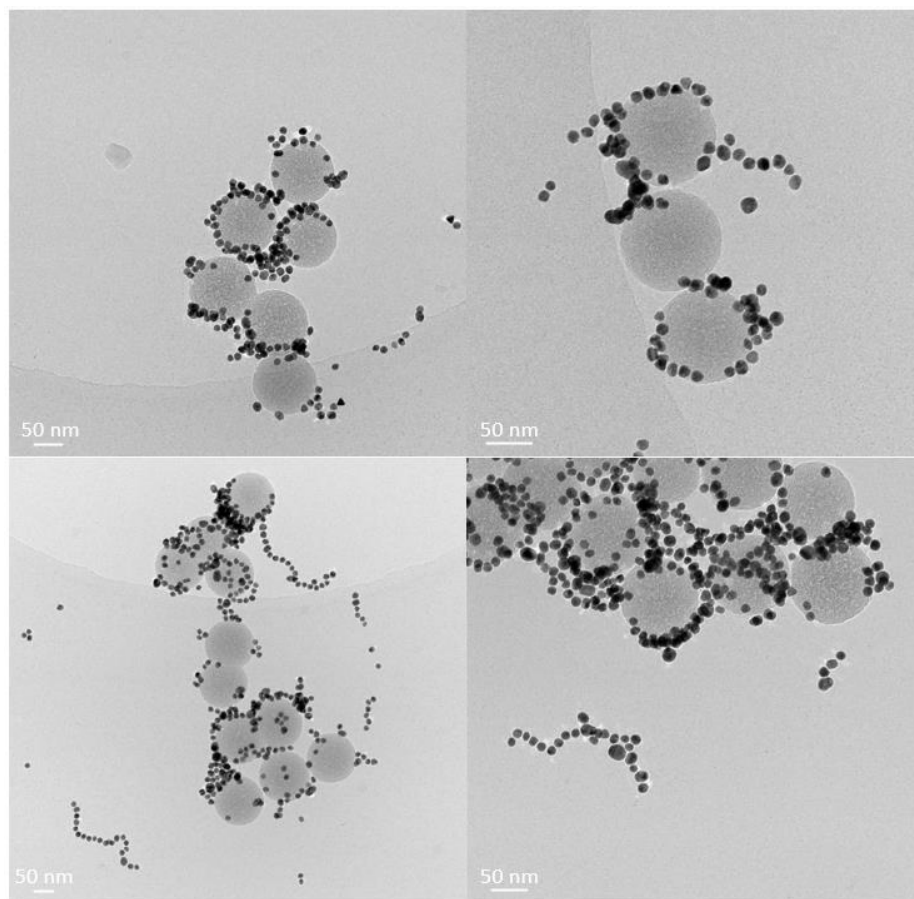


Figure S7: Cryo-TEM images of M-SiO₂NPs-AuNPs hybrids. M-SiO₂NPs are characterized by an almost complete membrane coverage (88%, estimated through ICP-AES).

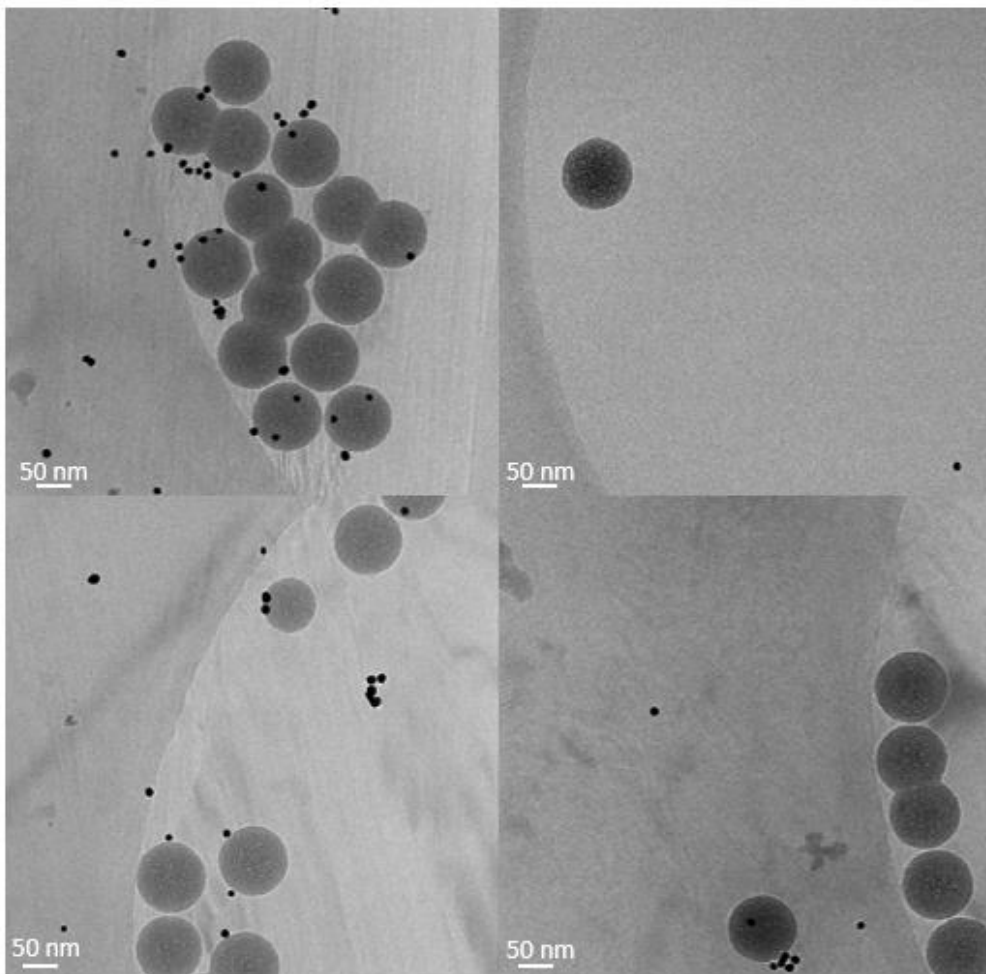


Figure S8: Cryo-TEM images of naked SiO₂NPs incubated with the AuNPs dispersion.

4.2 Dynamic light scattering

To gain more insights into the aggregation process, we performed DLS measurements on the very same samples used in cryo-TEM experiments. Figure S8 shows the normalized autocorrelation functions measured for the naked SiNPs, the naked SiNPs interacting with AuNPs, and the coated SiNPs interacting with AuNPs. The autocorrelation functions were analysed using a Non-Negatively constrained Least Squares fitting (NNLS). This model, generally used for polydisperse suspensions undergoing Brownian motion, provides a size distribution of the dispersed particles, reported in section figure S8. As shown, the hydrodynamic diameter evaluated for the naked SiNPs is centered at about 170 nm, according to reported cumulant fitting in the main text. The interaction of AuNPs with M-SiO₂NPs leads to the formation of larger hybrid objects with a hydrodynamic diameter of about 230 nm. Concerning the naked SiNPs-AuNPs sample, the correlation function

is bimodal, suggesting the presence of two separated populations presenting size distributions centred at 20 nm and 170 nm, respectively. Remarkably, the smallest population is consistent with the hydrodynamic dimensions of AuNPs, while the larger one shows very similar sizes to those measured for the uncoated SiNPs. The very fact that DLS measurements are consistent with the presence of two different populations, meaning that the dispersed objects possess very different diffusion coefficients, is a further confirmation that the interaction between AuNPs and SiNPs is mediated by the lipid coating.

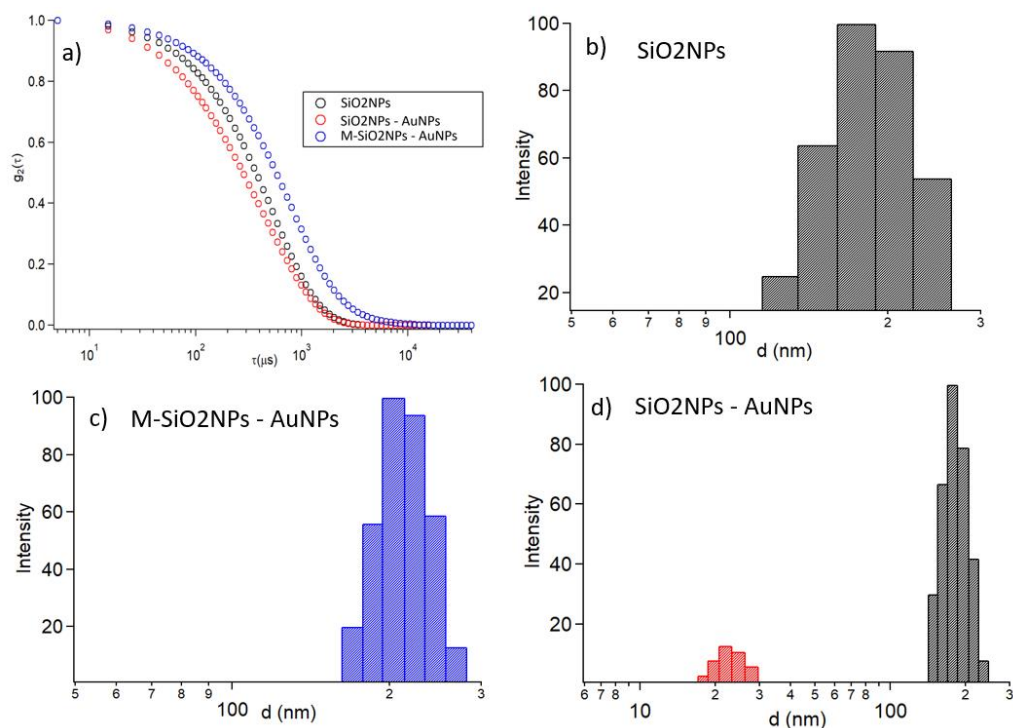


Figure S9: a) DLS autocorrelation functions of SiO₂NPs, SiO₂NPs – AuNPs, , M-SiO₂NPs – AuNPs, b) Size distributions obtained from the NNLS fitting of the DLS autocorrelation functions of diluted water dispersion of c) naked SiNPs, b) M-SiO₂NPs (with 88% membrane coverage)-AuNPs composites, and d) naked SiNPs-AuNPs mixture.

4.3 UV-vis spectroscopy

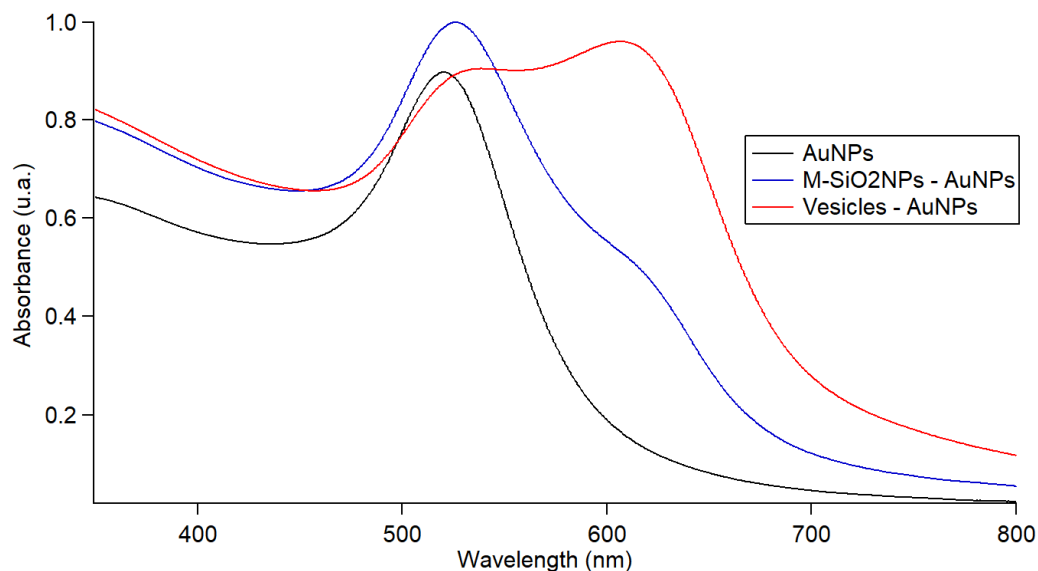


Figure S10: UV-vis spectroscopy comparing the plasmonic signal of bare AuNPs and AuNPs incubated with either M-SiO₂NPs (with 88% membrane coverage) or free-standing vesicles with the same lipid membrane composition. The concentration of AuNPs was 6.13 nM, while the concentration of vesicles and M-SiO₂NPs was 1.15 nM. The plasmonic variation of AuNPs interacting with M-SiO₂NPs is significantly less pronounced than the one observed for free-standing vesicles. This indicates a lower AuNPs clustering, likely due to the presence of the rigid silica core (absent in pristine liposomes), increasing the overall stiffness of the composite, in line with recent studies.^{3,4}

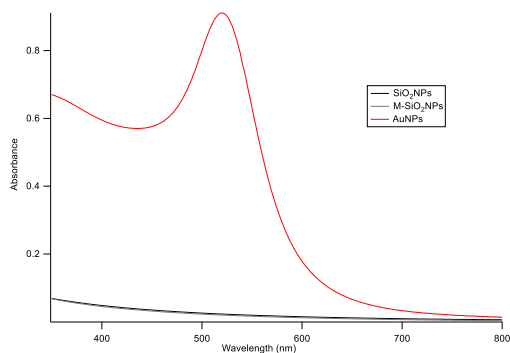


Figure S11: UV-vis spectra bare AuNPs (red profile) compared to the ones of SiO₂NPs (dark gray) and M-SiO₂NPs (with 88% membrane coverage, light gray). The concentration of AuNPs was 6.13 nM, while the concentration of SiO₂NPs and M-SiO₂NPs was 1.15 nM.

4.4 Small-Angle X-Ray Scattering

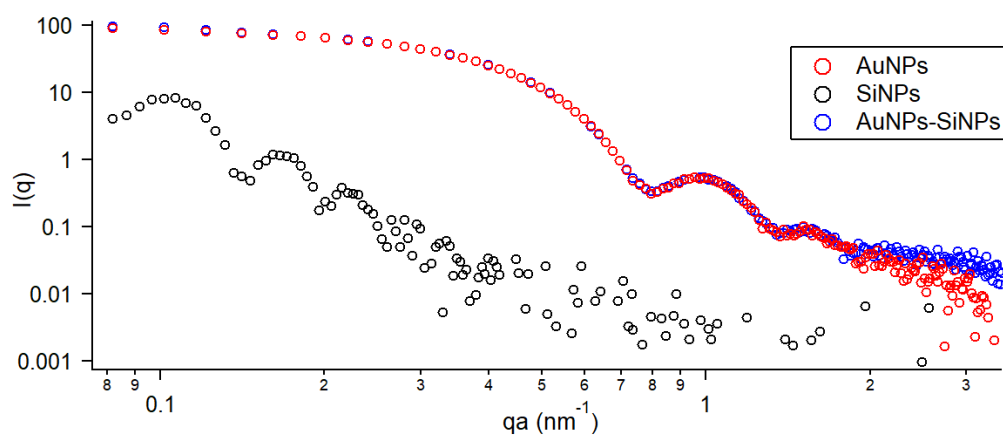


Figure S12: Comparison between SAXS profiles of bare AuNPs, SiO₂NPs, and SiO₂NPs -AuNPs mix obtained by adding 300 μ L of 6.13 nM of AuNPs to 50 μ L 1.15 nM of SiO₂NPs.

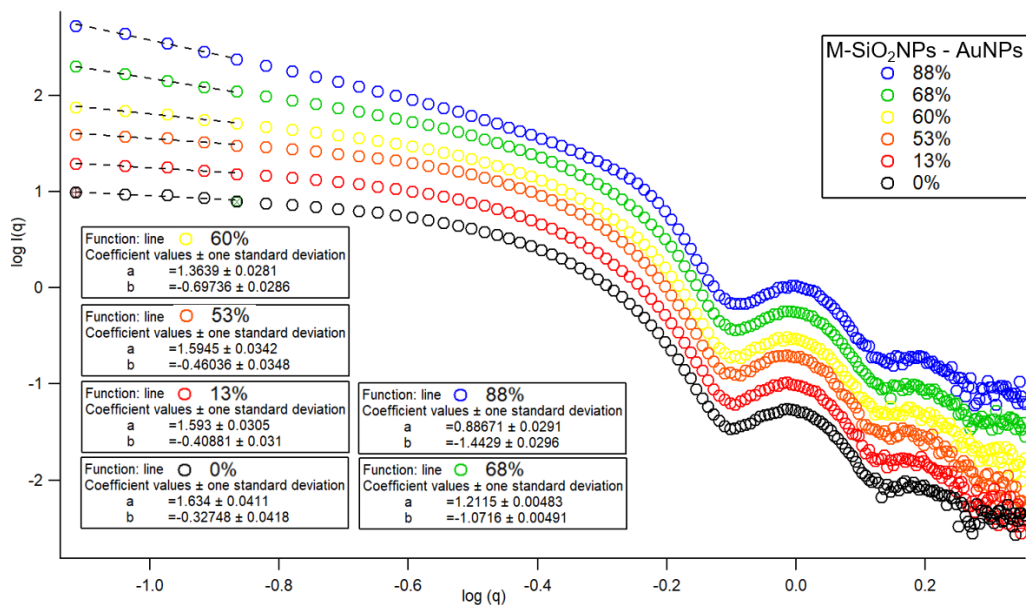


Figure S13: Log-Log SAXS profiles of M-SiO₂NPs-AuNPs mixtures with different degrees of SiO₂NPs membrane coverage collected after 10 minutes of incubation. The dashed lines represent the linear fitting in the Guinier region of the AuNPs ($0.082 < \text{nm}^{-1} < 0.161$). The “b” values in the squared boxes represent the slope values for the different SAXS profiles obtained from the fitting.

Sample	Porod coefficient
88%	1.44 ± 0.03
68%	1.07 ± 0.01
60%	0.70 ± 0.03
53%	0.46 ± 0.04
13%	0.41 ± 0.03
0%	0.33 ± 0.04

Table S3: Porod coefficient obtained from the slope of the linear fitting of the SAXS profiles in the low q region (Guinier region of the AuNPs $0.082 < \text{nm}^{-1} < 0.161$).

5 Characterization of the M-SiO₂NPs/AuNPs as a function of the degree of coverage

5.1 Dynamic Light Scattering

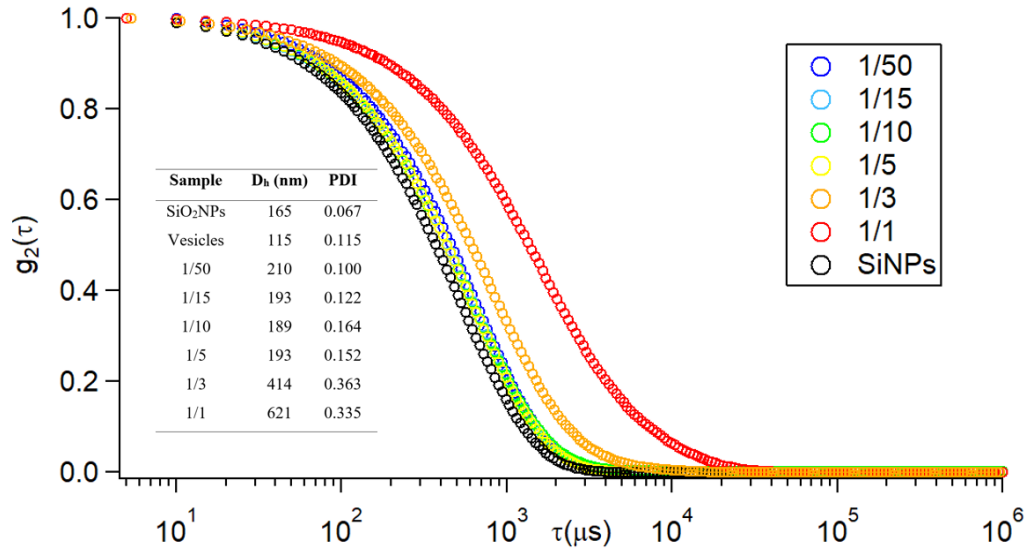


Figure S14: Normalized DLS curves obtained for M-SiO₂NPs with different coverages. The inset reports the hydrodynamic diameters and PDI of samples, showing the increase in the size of the samples with low coverages.

5.2 Nanoplasmonic assay for the quantification of the lipid coverage on SiO₂NPs

To set up a colorimetric assay for the estimation of the covered SiNPs (Figure S14), a quantitative descriptor of the plasmonic variations of AuNPs dispersion is required. With this purpose, we selected an aggregation index already used for quantifying the plasmonic variations induced by the presence of synthetic vesicles on the AuNPs dispersion⁴:

$$A. I. = \frac{A_{560-800}}{A.I._{AuNPs}}$$

Where $A_{560-800}$ is the area subtended by the absorbance spectrum in the 560-800 nm range, $A_{350-800}$ is the area of the entire spectrum, and $A. I._{AuNPs}$ represents the $\frac{A_{560-800}}{A_{350-800}}$ evaluated for the bare AuNPs dispersion.

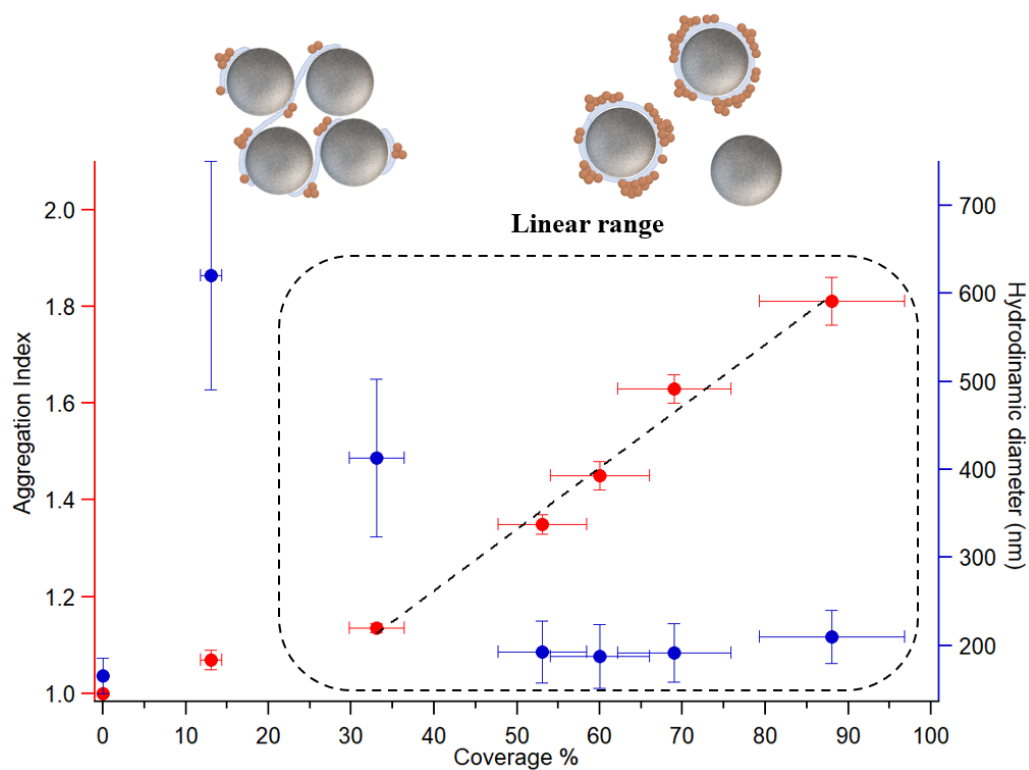


Figure S15: A.I. as a function of SiO₂NPs coverage. A.I. (left axis) and hydrodynamic diameter (right axis) as a function of SiO₂NPs membrane coverage (bottom axis). The linear fit for A.I. vs membrane coverage is also reported, in the 35-100% range of coverage, yielding a r-squared of 0.98.

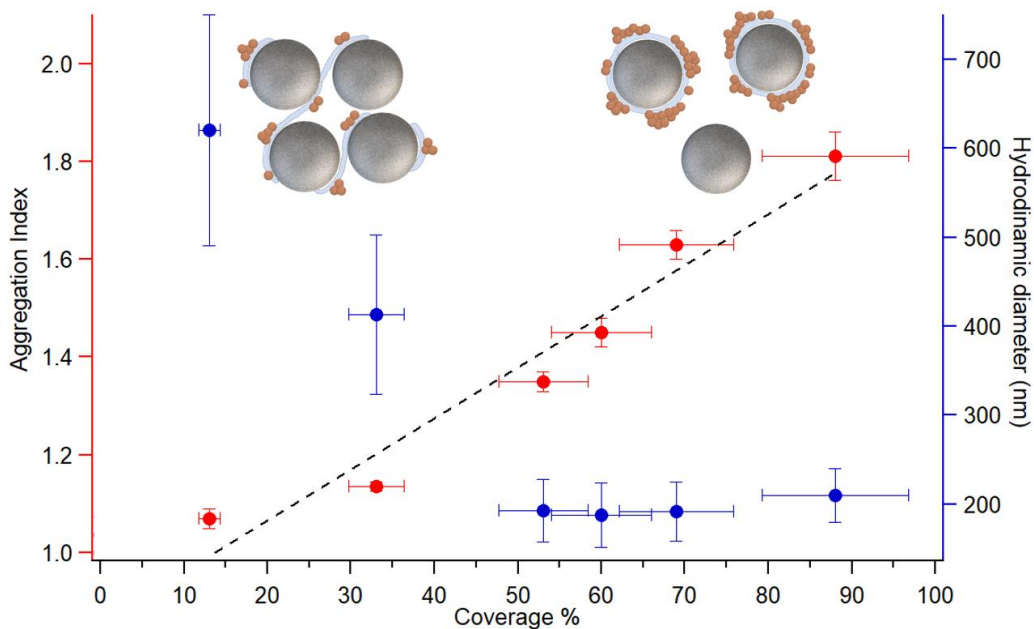


Figure S16: A.I. as a function of SiO₂NPs coverage. A.I. (left axis) and hydrodynamic diameter (right axis) as a function of SiO₂NPs membrane coverage (bottom axis). The linear fit for A.I. vs membrane coverage in the 13-100% range of coverage is reported. The goodness of fit decreases by the inclusion of the A.I. of the SiO₂NPs with a coverage of 13% (r-squared of 0.95).

Furthermore, to verify that the linearity of the spectral variation with the lipid coverage of SiNPs is independent of the selected A.I., we further analyzed the spectra with a different aggregation index (A.I. bis). Such A.I.bis was obtained as follow:

$$A.I. \text{ bis} = \frac{Abs_{max} - Abs_{600}}{\Delta\lambda}$$

Where Abs_{600} is the absorbance evaluated at 600 nm, Abs_{max} is the absorbance of the main peak of the dispersion, and $\Delta\lambda$ is the wavelength difference between 600 nm and the main peak. Each value is then normalized for the A.I. bis obtained from the bare AuNPs spectrum. This A.I. accounts of the spectral variation of the AuNPs spectra considering that the A.I. of bare AuNPs in always equal to 1 and, increasing the particle aggregation, the A.I. value decreases. Table S5 summarized the evaluated A.I.s for each coating extent.

SiNPs coverage	A.I.
88 ± 8 %	0.70 ± 0.05
68 ± 7 %	0.78 ± 0.03
60 ± 6 %	0.85 ± 0.03
53 ± 5 %	0.91 ± 0.02
33 ± 3 %	1 ± 0.01
13 ± 1%	0.99 ± 0.02
0 %	1

Tab S4: A.I. bis values obtained for each different membrane coverage of SiNPs.

By plotting the calculated A.I.bis versus the coverage of SiNPs the linear trend of the A.I. with increasing the SiNPs coverage is confirmed for the samples for the lipid coverages higher than approximately 35% (Fig S15).

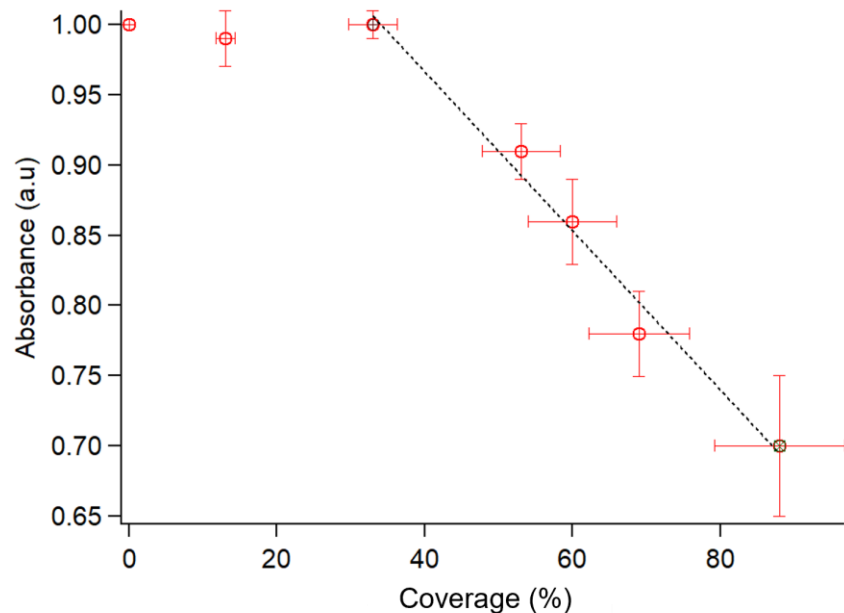


Figure S17: Linear trend of the A.I. bis as a function of SiNPs coverage. The samples with low surface coverage (<35%) cannot be fitted by the linear regression.

References

- 1 W. Haiss, N. T. K. Thanh, J. Aveyard and D. G. Fernig, 2007, **79**, 4215–4221.
- 2 X. Liu, M. Atwater, J. Wang and Q. Huo, 2007, **58**, 3–7.
- 3 J. Cardellini, L. Caselli, E. Lavagna, S. Salassi, H. Amenitsch, M. Calamai, C. Montis, G. Rossi and D. Berti, *J. Phys. Chem. C*, 2022, **126**, 4483–4494.
- 4 L. Caselli, A. Ridolfi, J. Cardellini, L. Sharpnack, L. Paolini, M. Brucale, F. Valle, C. Montis, P. Bergese and D. Berti, *Nanoscale Horizons*, 2021, **6**, 543–550.